Article:

Garum, M orcid.org/0000-0002-4703-4350, Glover, PWJ orcid.org/0000-0003-1715-5474, Lorinczi, P et al. (2 more authors) (2021) Ultrahigh-Resolution 3D Imaging for Quantifying the Pore Nanostructure of Shale and Predicting Gas Transport. Energy & Fuels, 35 (1). pp. 702-717. ISSN 0887-0624

https://doi.org/10.1021/acs.energyfuels.0c03225

Ultrahigh resolution 3D imaging for quantifying the pore nanostructure of shale and predicting gas transport

Mohamed Garum[1], Paul W.J. Glover[2], Piroska Lorinczi[2], Gilbert Scott[3], Ali Hassanpour[1]
[1]School of Chemical and Process Engineering, University of Leeds, Leeds LS2 9JT, U.K.
[2]School of Earth and Environment, University of Leeds, Leeds LS2 9JT, U.K.
[3]School of Engineering, University of Aberdeen, Aberdeen, AB24 3FX, U.K.

Abstract

Pore and fracture microstructure is key to understanding gas flow in shales. The experimental determination of these microstructures is dependent on the measurement technique employed and its resolution. High-resolution three-dimensional imaging techniques coupled with image analysis and direct numerical simulations have been employed to characterise the petrophysical properties of shale samples. In this work our particular focus is on using the Nano-CT and FIB-SEM techniques at the same location in a shale rock sample in order to investigate the effect of their different resolutions and fields of view on the resulting imaged nano-pore structure, as well as to determine any differences in the consequent measurements of the shale petrophysical properties. These petrophysical properties include porosity, permeability, pore volume and size distribution, pore aspect ratio, surface area to volume and pore connectivity. The reconstructed matrix, kerogen and pore space volumes from each approach showed significant scale-dependent differences in microstructure. The shale sample displayed a high kerogen content with high connectivity. Porosity from the reconstructed shale volumes was observed to be 0.43% and 0.7% for FIB-SEM and Nano-CT approaches, respectively. Pore volume, size, surface area to volume ratio and two orthogonal pore aspect ratio distributions have also been extracted from the reconstructed image data by 3D image analysis. These data show that voids within the rock are oblate at all scales. Permeabilities have been calculated from both the FIB-SEM and Nano-CT images and fall in the range 2.55 nD to 9.92 nD. A simulation has also been produced based on the permeability calculation and parameters from the image analysis. The results of the simulation of the show connectivity in the x-, y- and z-directions for both the FIB-SEM and Nano-CT images, with very low connectivity in the x-direction, but higher connectivity in the y- and z-directions.

1. Introduction

Prediction of gas transport capacity is one of the most critical considerations in the development of shale gas reservoirs, affecting commercial scale shale gas production significantly [1]. It is vital to estimate the shale gas resources and long-term production strategies because the microstructural properties of the shale (e.g., pore volume, size distribution, and pore connectivity) control fluid transport through the shale [2]. These properties are controlled by differences in the origin, size, shape and connectivity of the pores, which in turn lead to differences in their contribution to gas storage and permeability [3, 4]. Consequently, a better knowledge of these properties will lead to a better understanding of the pores, organic matter and mineral distributions in the shale, and will also provide a basis for understanding gas storage and transport mechanics in shale [5]. Gas transport through shale is a very complex process, operating at multiple scales and encompassing multiple, often poorly understood, flow mechanisms. This is mainly because the sizes of pores and fractures in shales vary over many orders of magnitude; from only a few nano-meters to several tens of microns [6, 7, and 8]. Consequently, the pore networks cannot be imaged effectively using a single technique with a given resolution and field of view. A number of different imaging techniques each with its own resolution and field of view, must be used, instead.

Shales generally have low porosities and extremely low permeabilities [2]. The quantification of the porosity and permeabilities of prospective gas shales is a major challenge for industry [9]. This is partly because both the porosity and permeability are numerically small, but also because the state of the rock *in-situ* (saturated with water and at raised temperatures and pressures) may be very different from that when measured in the laboratory (dry, fractured, plated and at laboratory temperatures and pressures).

Extensive research efforts have been carried out on this topic mainly based on the conventional experimental investigations of shale core plugs with the pulse-decay method to quantify the shale permeability [10, 11, 12]. These investigations have involved the measurement of the impact of pore pressure and confining pressure on the shale permeability [9, 13, 14, 15, and 16]. Many other investigations have reported the estimation of the permeability by using crushed shale samples (e.g., [17]). This method only determines the apparent permeability of shale matrix, which removes the presence of microfractures and the impact of stress [10, 18, and 19]. However, due to the limited accuracy and considering the excessive time needed for experimental design, permeability can only be considered phenomenologically within conventional experimental methods.

On the other hand, the characterization of the pore microstructure in shale is key for investigations of the fluid transport, considering that the pore size distribution (PSD) in shale ranges from subnanometers to micrometers [20]. Shale contains multiscale pores, commonly regarded in the literature as micropores (<2 nm), mesopores (from 2 to 50 nm), and macropores (>50 nm) [20]. Other researchers have used different classification schemes for pore size. For example, [21] and [22] classify pore size as picopores (<1 nm), nanopores (from 1 nm to 1 μm), and micropores (from 1 μm to 65.5 μm). In this paper, we use the Josh [20] classification.

A number of imaging techniques have been used recently for the analysis of porosity and permeability in shales, including Focused Ion Beam Scanning Electron Microscopy (FIB-SEM) and X-Ray Tomography with a micrometer-scale resolution (Micro-CT) or with a nanometer-scale resolution (Nano-CT). Figure 1 shows a comparison of the resolutions and dimensions of imaging using Micro-CT, Nano-CT and FIB-SEM techniques. These techniques have been shown to be powerful tools for resolving petrophysical issues, including the visualisation of fine microstructure [23], the quantification of the size, size distribution and morphology of the shale phases (mineral matrix, pores and organic matter), and the 3D connectivity of the shale components that ultimately controls the ability of the pore network to transport gas [24, 25, 26].

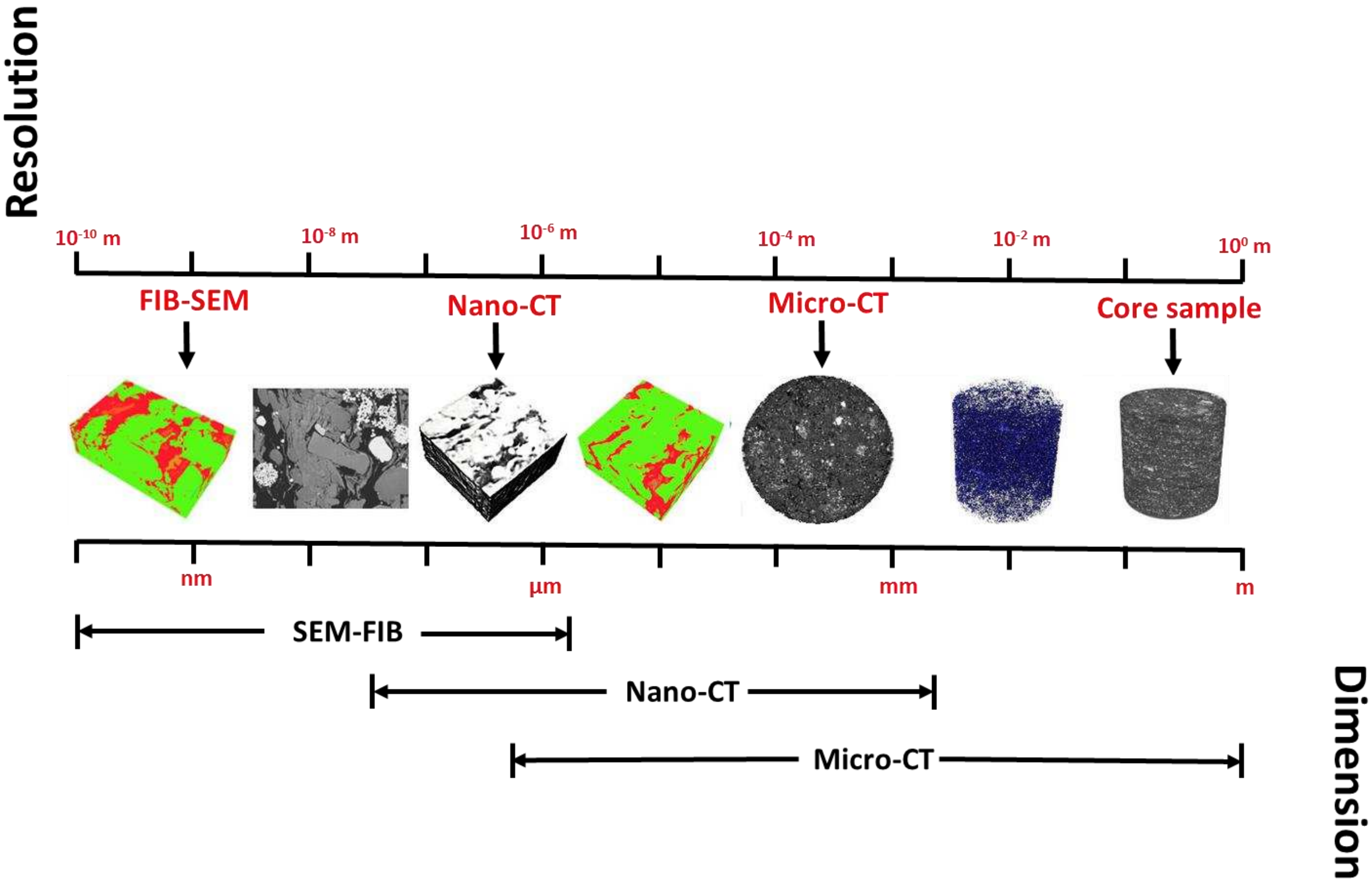

Figure 1. Multiscale imaging techniques (FIB-SEM, Nano-CT and Micro-CT) used in this study.

However, these techniques have their own limitations in terms of resolution and sample size. For example, the Micro-CT and Nano-CT techniques can only determine the pore throats larger than 0.7 µm and 0.05 µm, respectively [23]. These techniques show many pores to be either isolated or only connected locally [15, 23, and 27]. However, since the shale is permeable we can infer that some pores are pervasively connected and if no such connectivity is seen at the larger scales then that connectivity must occur at smaller, sub-resolution, scales [7, 20], and that permeability can be measured by pulse decay techniques. By contrast, the FIB/SEM approach can resolve the pores from 10 nm to 50 µm [27], often showing reasonable inter-pore connectivity.

In contrast, imaging techniques with high resolutions have a very small 3D field of view, placing an upper limit on the size of pores they can image effectively. For example, the FIB-SEM method has an absolute upper limit of 15 µm in this work, which can be much smaller if the imaged pores are very oblate, and in shales. Consequently, ideally a number of imaging techniques need to be used in order to cover the range of resolutions and 3D fields of view if the full texture of the shale is to be captured, and those imaging techniques should be carried out on exactly the same volume of rock.

In this study, we have characterised a single rock sample from a shale reservoir using two three-dimensional techniques at nanoscopic scale on "exactly the same volume of rock" for the first time. Previously, different techniques with different resolutions could only be applied to separate samples from a close common source such as from the same core. However, variability between these samples at a fine scale meant that it was not previously possible to associate differences between the measurements with changes in resolution because microstructural differences between the samples existed.

In our case, small cubic core samples (25 µm side length) were prepared from reservoir rocks using a Focused-Ion Beam (FIB) milling technique. The pores inside the sample were first characterized using ultra-high resolution image obtained at an initial state by non-destructive X-ray nano-tomography (Nano-CT), and we subsequently used the same location within the original sample volume for FIB-SEM higher resolution at the nanometric scale. The FIB-SEM imaging destroys the sample. This approach has a number of advantages. The first advantage is that FIB sample preparation allows the same sample to be imaged by two different high resolution techniques with minimal damage during preparation. This enables us to understand which aspects of the measurements are native to the specimen and which are caused by preparation for all measurements, irrespective of scale, resolution and field of view. The second advantage is that the Nano-CT and FIB-SEM measurements can be made at exactly the same predetermined location in the sample, chosen to investigate a particular feature or to represent a typical location within the sample. The third advantage is that the characteristics of imaging a particular structure with each of the imaging techniques can be compared directly. Consequently, it is possible to distinguish between observations which are related to the imaging technique and those which arise from the sample itself. In the latter case, differences in the results of the two imaging techniques may be used to investigate the variability of heterogeneity and anisotropy of pore and kerogen distributions as a function of scale, and hence estimate their connectivity.

2. Material and Methods

2.1 Rock samples and preparation

The gas shale samples used in this study were collected from a depth of 110 m in a gas shale formation in Sweden. At the time of the study this was the sole source of gas shale reservoir material available to us. However, due to confidentiality, the sample used has been coded Sample A. This sample has been imaged and analysed in this study using two different high-resolution imaging techniques, with the primary aim of understanding the microstructure of the shale, including the porosity and permeability, pore volume and size distribution, and the secondary aim of comparing the results of the two techniques when imaging the same microvolume of rock.

The two techniques we used in this study are X-ray Nano-Computed Tomography scanning (Nano-CT) and a combination of scanning electron microscopy using a focused ion beam to successfully strip material from the surface between scans (FIB-SEM). In our implementation, imaging has been possible with both techniques on a single sample with a characteristic size of 15-25 µm. High resolution imaging such as that carried out in this work requires very small samples, in order to scan and mill the same region for both techniques, whose preparation is time-consuming and requires significant care. The higher the resolution we require, the smaller the samples must be.

The samples are required to be suitably thin in order to produce high-quality images using Nano-CT and FIB-SEM. The mechanical crushing or laser milling of the samples does not produce samples of the correct size. Furthermore, it can cause damage to the pore network within samples. By contrast, ion milling technique can prepare very small samples with minimal damage to the pore-space, and is consequently ideal for the preparation of shale samples for high resolution 3D imaging [28].

The stepwise preparation process we have developed is shown in Figure 2. Sample A was prepared using a dual beam FIB-SEM system from an original core sample of around 3 mm in length and diameter. The core sample was initially sub-divided to produce cubes of side-length approximately 1 mm using a diamond saw. One of these 1 mm-sized cubes was loaded into the dual-beam FIB-SEM apparatus and a region of interest (25×25 μm^2) was identified using scanning electron microscopy. The region of interest was then coated with a thin protective layer of platinum to offer protection and mitigate specimen charging (typically 1 µm in thickness; Fig. 2a). Subsequently, the rock volume around the platinum layer was removed by FIB milling with a 30 kV Gallium ion beam energy and a 2.5 nA beam current (Fig. 2b-c). In the next step, the top of the sample was carefully attached to the tip of a micromanipulator using platinum welding (Fig. 2d). The resulting isolated cubic shape was cut free from the bulk rock using FIB milling (Fig. 2e). The height of the resulting cube was typically 1–2 times greater than the diameter of the micromanipulator. In the final step, the bottom of the cube was attached to a needle by platinum welding and the micromanipulator was cut free by FIB milling (Fig. 2f-g). The outcome of this process was a cube of side-length about 25 µm placed on the tip of a needle (Fig. 2h-i), which was mounted on a sample holder for Nano-CT measurements, and then the same area was used for FIB-SEM imaging (Fig. 3).

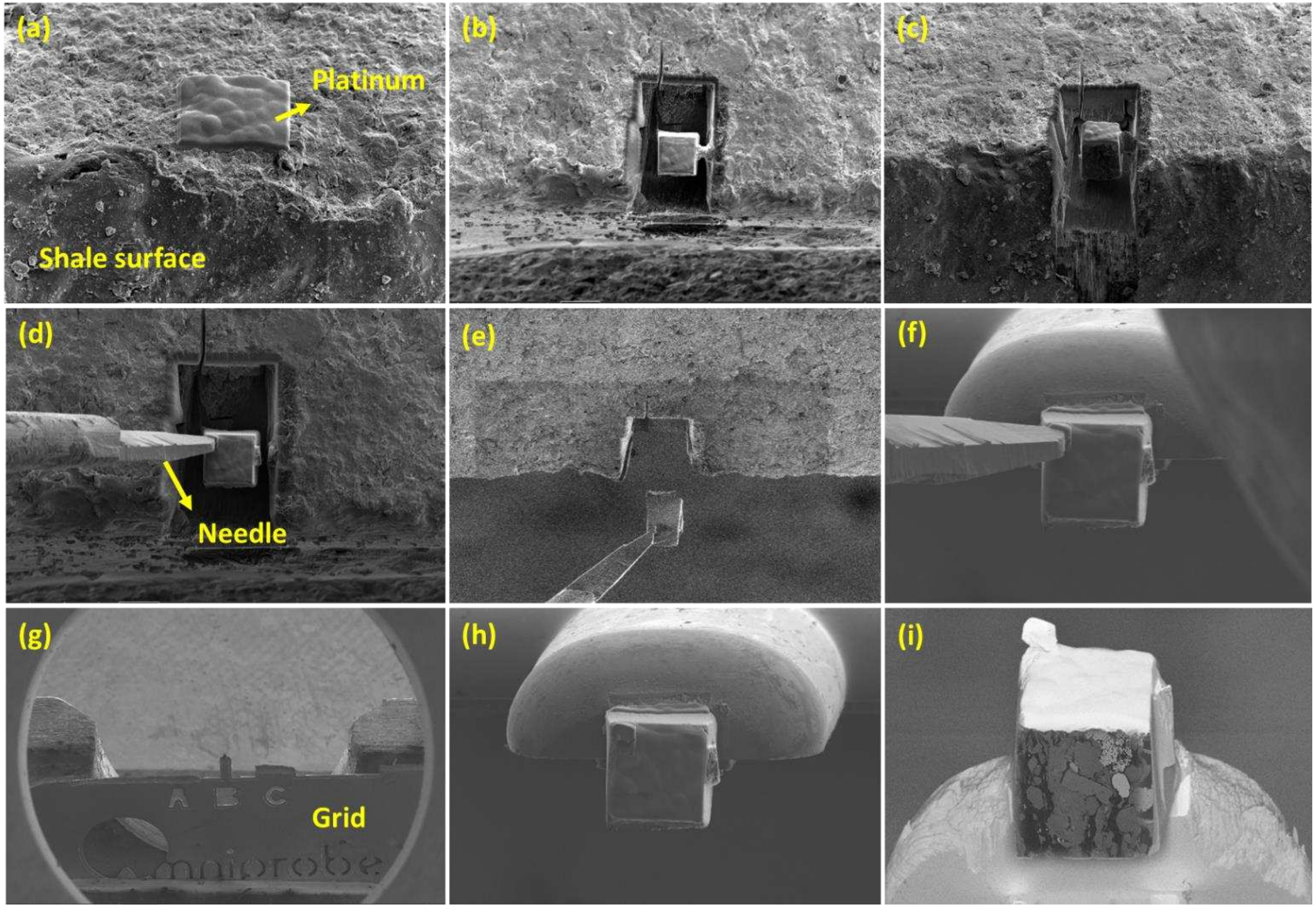

Figure 2. Sample preparation for Nano-CT and FIB-SEM using FIB milling and micromanipulation: (a) the surface of shale rock on which the region of interest is shown coated with Pt, (b-c) mill out the area around the sample, (d) attach the sample to the tip of a micromanipulator, (e) cut the cube free from the bulk rock, (d-h) weld the bottom of the cylinder to the tip of a grid (here the samples is the small dark point on Grid Position B), (i) The final sample (region of interest) is approximately 25×25 μm^2.

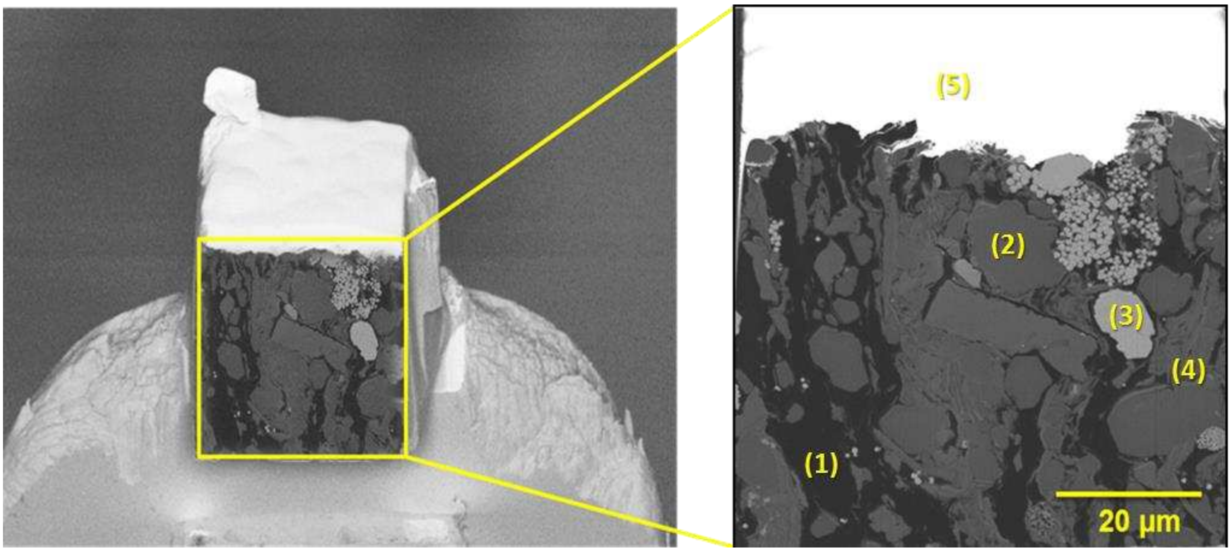

Figure 3. Shale rock sample A for Nano-CT and FIB-SEM imaging. (1) Dark grey, kerogen; (2) medium grey, silicate matrix; (3) light grey, iron pyrites, often in framboidal form. (4) Pores (black) are too small to be seen at this resolution. The covering of the sample which appears white is the layer of Pt (5) that was initially deposited at the start of the sample preparation process ([29]).

2.2 Experimental procedure

Nano-computed tomography (nano-CT) and Focused Ion Beam and Scanning Electron Microscope (FIB-SEM) were performed in this work with the primary goal of imaging and understanding the petrophysical structure of the shale at exactly the same location of the sample. The imaging was done in three-dimensions, and three-dimensional image analysis has been carried out to obtain a range of petrophysical characteristics, including the porosity, pore volume and pore size distributions, as well as allied parameters relating to kerogen. These parameters allow a rudimentary calculation of permeability to be carried out. In each case, we have compared the results obtained from each of the Nano-CT and FIB-SEM approaches.

The Nano-CT instrument used in this study was the ZEISS Xradia 810 Ultra, at the University of Manchester. The X-ray source on this instrument provides an X-ray beam of 35 keV energy with a power of 7 watts. The instrument provides imaging pixel resolutions of 64 nm with 1601 projections, and the time exposure of each scan is about 90 sec.

The Nano-CT system consists of a highly-collimated X-ray source, a rotation stage to mount and control the sample, and an X-ray detector. X-rays generated by the source pass through the sample and are recorded by the detector. The distance between the sample and both the source and the detector are critical parameters for the accurate reconstruction of the three-dimensional properties of the sample.

The dual ion beam (FIB-SEM) system (FEI Helios G4 CX DualBeam) allows a sample to be cross-sectioned and imaged *in-situ* using 30 keV electrons from an integrated SEM with a pixel resolution of 36×45 nm. The FIB milling removes material from the surface of the sample (Figure 3), giving the SEM access to a new surface to image. Reiteration of imaging and milling, a process known as “slice and view”, allows a 3D volume of the rock sample to be imaged. During the milling, the SEM beam is kept normal to the sample surface and the FIB ion beam is usually set at an angle of 52°. The milling uses an ion beam voltage and current of 5 kV and 4 nA, respectively, and on each occasion the FIB mills away a slice of material approximately 20 nm thick. This milling and imaging process is repeated, typically 750 times and the resulting voxel size for this work is approximately 36×45×20 nm^3, with a typical imaged volume of 25×25×15 μm^3. Figure 4 shows images of the sample visualised by each of the two methods.

Energy dispersive spectroscopy (EDX) was also performed to investigate the elemental composition and mineralogy of the shale microstructure characteristics (Figure 5). The EDX system uses a detector to collect the X-ray signals generated from the sample by the electron beam. The energies of the X-rays generated are characteristic of electron level transition in the atoms irradiated. This provides a way to correlate the spatial position of the microstructure with elements of the composition using the same electron beam.

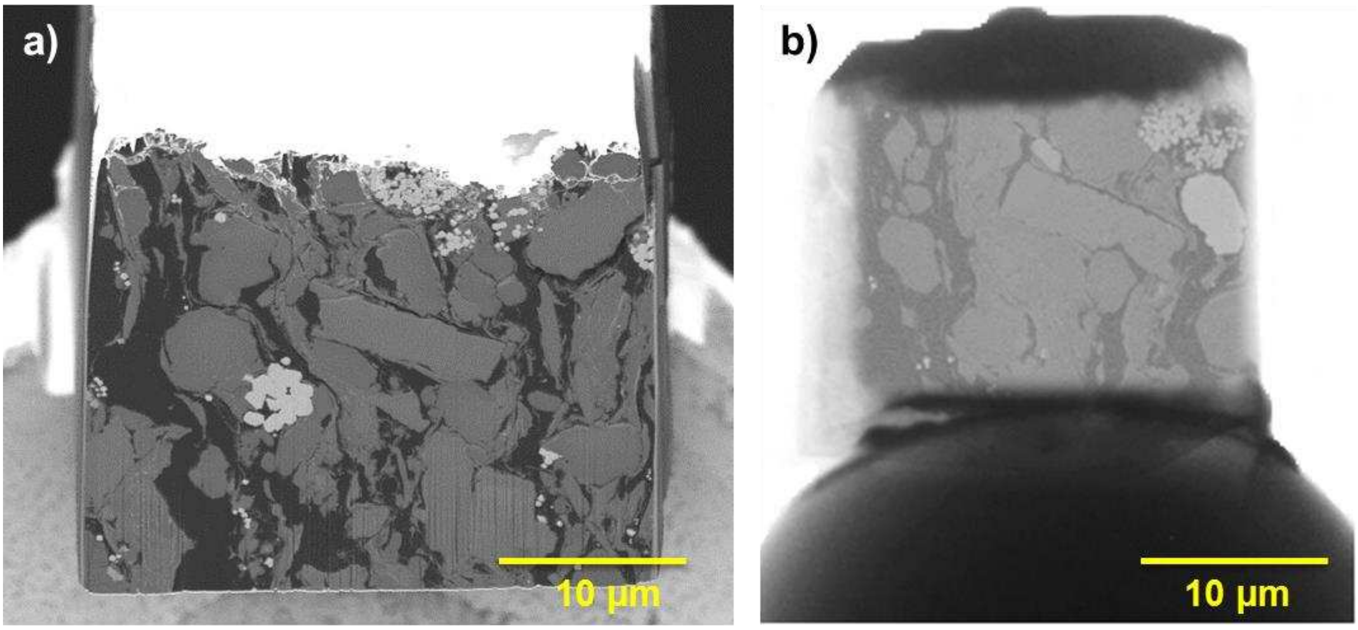

Figure 4. (a) Image of the sample using the FIB-SEM technique (face dimensions 25×25 μm^2), (b) 3D image of the sample using Nano-CT scanning for the same shale sample.

Figure 5 shows an EDX mapping of the region of sample shown being prepared in Figure 3 with individual distributions of the main elemental compositions; where (Si) is silicon, the area shown in yellow is sulfur (S), the green is oxygen (O), carbon (C) is shown in red, and the pink is potassium (K). Close observation of the SEM/EDX images shows very small vertical stripes (Figure 4a and 5). This is an artefact known as curtaining which is caused by the ion beam during milling. Curtaining is a major problem when using a broad ion beam milling and is less apparent when milling with a focussed ion beam. Nevertheless, curtaining can affect elemental mapping, as seen particularly in the panel representing oxygen in Figure 5, as well as affecting the segmentation process and having some impact upon subsequent image analysis results.

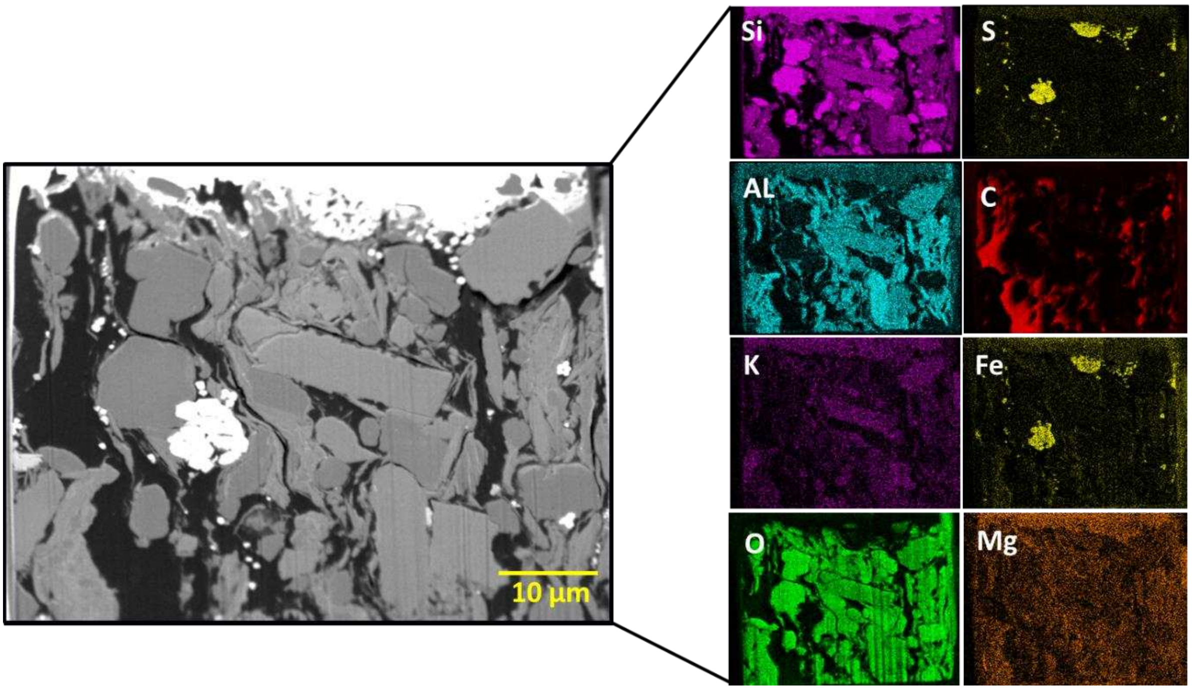

Figure 5. An EDX map of a cross-section of the shale sample used for elemental mapping, where the clastic matrix (high Si, Al, K, O) can be distinguished from the kerogen (high C), and the framboidal iron pyrites are clearly shown by their associated high sulphur (S) values ([29]).

2.3 Nano-CT and FIB-SEM Imaging Parameters

The 3D visualisations from each approach were image-analysed in three-dimensions to provide values of porosity and kerogen fraction, pore and kerogen size and volume distributions, pore shapes, aspect ratios, and surface area to volume ratios. The microstructural characteristics arising from both Nano-CT and FIB-SEM approaches have been compared in order to provide more understanding with regard to the effectiveness of each technique in capturing the microstructure of shales. In addition, these techniques are compared based on their respective field of view, resolutions, advantages and disadvantages. Table 1 summarizes the main characteristics for each technique, including the experimental parameters used in this study.

Table 1. Comparison of the operational parameters of the Nano-CT and FIB-SEM techniques (as implemented in this work).

Aspect	Direction	Nano-CT	FIB-SEM
Imaging time (hours)		40	5-8
Resolution (nm)	x	64	36
	y	64	45
	z	64	20
No. of projections or slices	z	1601	750
Sample survival		Non-destructive	Destructive
Imaging conditions		Atmospheric	Vacuum
Considerations		Low contrast	Excessive brightness

2.4 Data processing and reconstruction

The Nano-CT and FIB-SEM imaging processes each create a stack of 2D images composed of pixels of different grayscale values. Both Nano-CT and FIB-SEM images usually contain artefacts and noise which can affect image processing adversely, particularly affecting segmentation. We have used a "Non-Local Means filter" [30], implemented in Avizo® Fire 9.40 software, in order to reduce the effect of imaging artefacts and noise. The resulting images from both methods were segmented using manually chosen thresholds in order to distinguish between the pore-space and kerogen based on individual pixel grey-scale levels [30, 31, 32, 34]. This process produces a set of 2D binary files for each image, each of which maps the presence of one of the segmented phases; matrix, kerogen and porosity in this work. These binary files, when stacked, provide 3D binary data volumes for each phase. Either the 2D or 3D binary data files can be subjected to image analysis, which we have carried out with Avizo® Fire 9.40 software.

Avizo® Fire 9.40 software was used to calculate a range of microstructural parameters, including porosity, kerogen fraction, pore size distribution, and parameters describing the morphology of pores and kerogen. Figure 6 illustrates (a) 2D raw grayscale image, (b) the result of applying a non-local means filter to the same 2D grayscale image, (c) the segmented image with three phases where pores are shown in blue, kerogen is presented in red and matrix is shown in light green, and (d) a magnified area within the segmented image with a finer pixel size revealing better-defined boundaries between the pores (blue) within the kerogen (red) and mineral (green) phases.

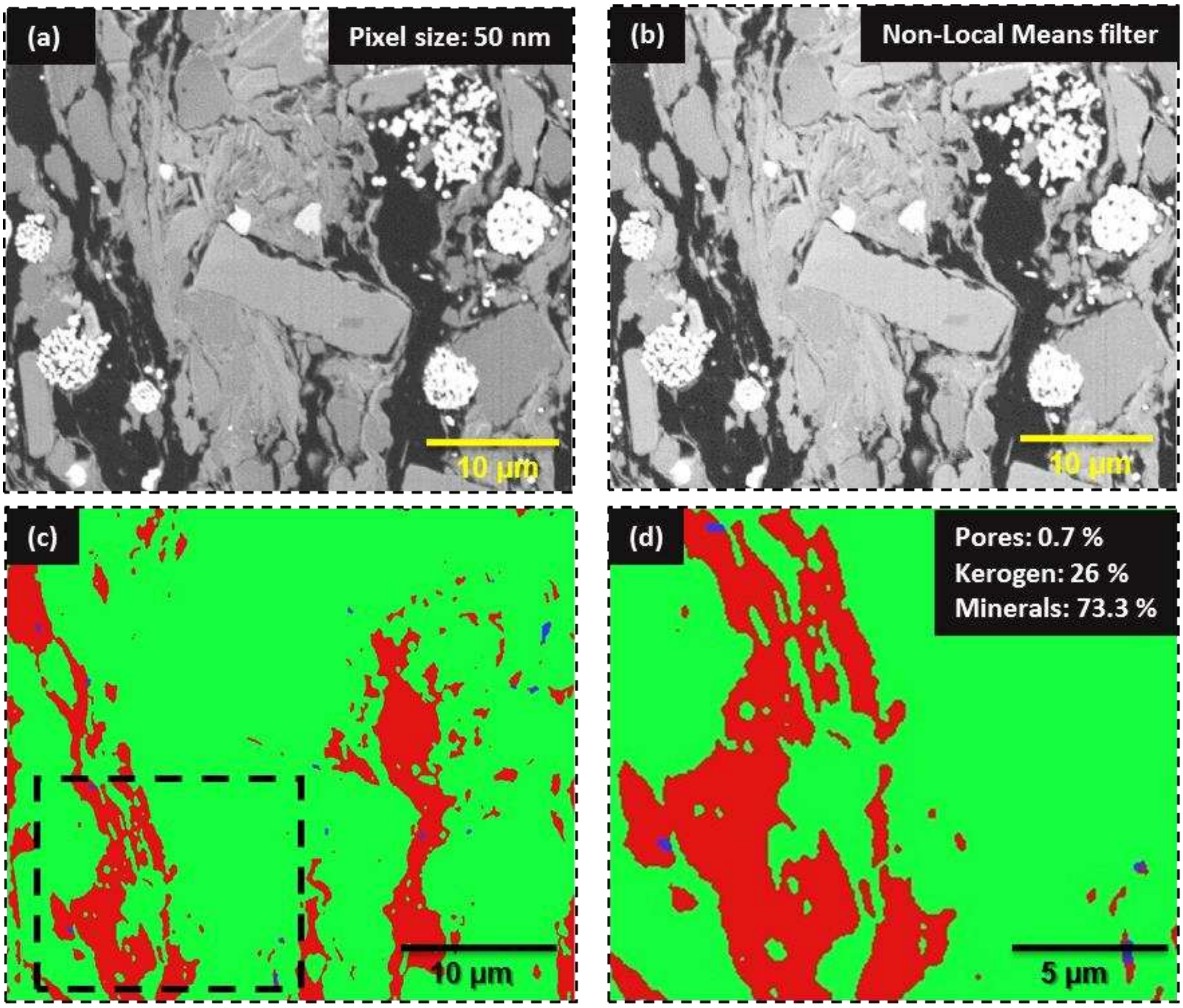

Figure 6. Backscattered electron (BSE) images of the shale rock sample of the region of interest: (a) 2D raw grayscale image, (b) result of applying a non-local means filter to the same 2D image, (c) segmented image with all phases, where pores are blue, kerogen is red and the matrix minerals are shown in light green, (d) a magnified area within segmented image revealing more well-defined the pores in the kerogen and mineral phases.

2.5 Supporting measurements

A number of different supporting measurements have been used in this study.

Mercury intrusion porosimetry (MIP) was carried out on associated rock samples to provide independent values of pore throat size, pore size, grain size, pore volume and porosity, as well as capillary pressure [34]. During MIP measurements, mercury is injected into the pore spaces through connected paths under progressive and stepwise increases in pressure up to 60,000 psi, while measuring the intruded mercury volume at each step. At the highest pressures the Washburn equation [35] predicts that mercury should pass through pore throats down to 3 nm [36], which in principle provides data to a smaller scale than may be imaged. While the data provides a useful comparative dataset, there is significant concern [37] that it may significantly both underestimate and overestimate the pore volumes within shales. Underestimations arise because shales are significantly compressible. The imposition of an external 60,000 psi pressure would be sufficient to close many of the pore spaces the technique is supposed to be measuring, particularly the high aspect ratio pore spaces which are common and critical in the shale pore microstructure. Overestimations may arise from measurement-induced fracturing caused by the imposed stresses. In our measurements we found that this method systematically produced larger porosities than the values obtained from our two imaging techniques.

Pulse decay permeametry (PDP) has been used to measure the permeability and porosity of associated samples of rock experimentally [38]. The technique relies on analysing the transient pressures associated with the decay of a pressure pulse which applied to the sample [10]. The pressure decay curve obtained from the test is used to determine the porosity and permeability [39]. The range of permeabilities which may be measured using this method is between 0.1 mD and 10 nD [12].

The Gas Research Institute (GRI) method is another technique used for measuring porosity and permeability which also relies on gas pressure decay, but in this case the sample is crushed [10, 40]. The pressure is recorded as a function of time, and porosity and permeability can be found from the pressure and time data as gas flows into the shale [19]. The range of values of permeability that can be measured using this technique is typically in the nD range [19].

3. Results

In this article the 3D reconstructions data were acquired by using Nano-CT and FIB-SEM techniques within an imaged volume of $25\times25\times25$ μm^3, which makes them very suitable for testing the limitations of Nano-CT and FIB-SEM with regard to shale properties. A wide range of microstructural parameters were calculated for both datasets and compared against each other, including porosity and permeability, together with pore and pore throat size distributions, two aspect ratios and scale-independent surface area to volume ratios. Table 2 shows a brief summary of the most important of these results.

Table 2. Comparison between the two imaging techniques of the main parameters measured in this paper.

Sample	Technique	Voxel size (nm)	Sample Size (μm)	Measured Porosity (%)	Measured Kerogen (%)	MIP Porosity (%)
A	Nano-CT	64×64×64	25×25×25	0.43±0.04	19.6±0.8	1.8±0.09
	FIB-SEM	36×45×20	25×25×15	0.70±0.07	26.0±1.3	

3.1 Comparison of 3D-dimensional microstructure results

A comparison of three-dimensional microstructure sub-volumes of the shale rock sample has been performed based on the Nano-CT and FIB-SEM images of sections through the sample (Figures 7 and 8). In both cases, the analysis was carried out with voxels representing the corresponding resolution. The FIB-SEM dataset is smaller than a Nano-CT volume in terms of pixels because only that 15 μm of the 25 μm available in the *z*-direction was accessed by the 750 slices we used.

Figures 7 and 8 show 3D images obtained from Nano-CT and FIB-SEM with important parameters relevant to gas transport such as pore, kerogen, and matrix phase fractions. By using the 3D grayscale of the raw data of these two techniques, threshold values can then be set to define microstructural features of interest, particularly the pores, kerogen and other minerals (the lighter equant patches are framboidal pyrites). Surfaces can then be generated around these regions within the thresholds. Figures 7b and 8b show images of the 3D reconstructions of the solid material for Nano-CT and FIB-SEM. After this has been accomplished, we have been able to separate the material based on grayscale values. Figures 7c-e and 8c-e show the 3D images of the pores, kerogen and other minerals, respectively. Based on this thresholding process, a qualitative inspection of the connectivity of the networks can be performed. It can be observed that the FIB-SEM presents a higher value for pores and kerogen than the Nano-CT, and also there is a higher degree of pore and kerogen connectivity across the volume (*cf.* Figure 8c-d and Figure 8c-d).

In addition to the qualitative analysis of the 3D microstructure, quantitative estimates of the percentage volume of these features can be calculated. The estimates obtained, by percentage volume of pores, kerogen and minerals in the reconstructions are 0.43%, 19.60% and 79.97% for Nano-CT, and 0.70%, 26.00% and 73.30% for FIB-SEM respectively.

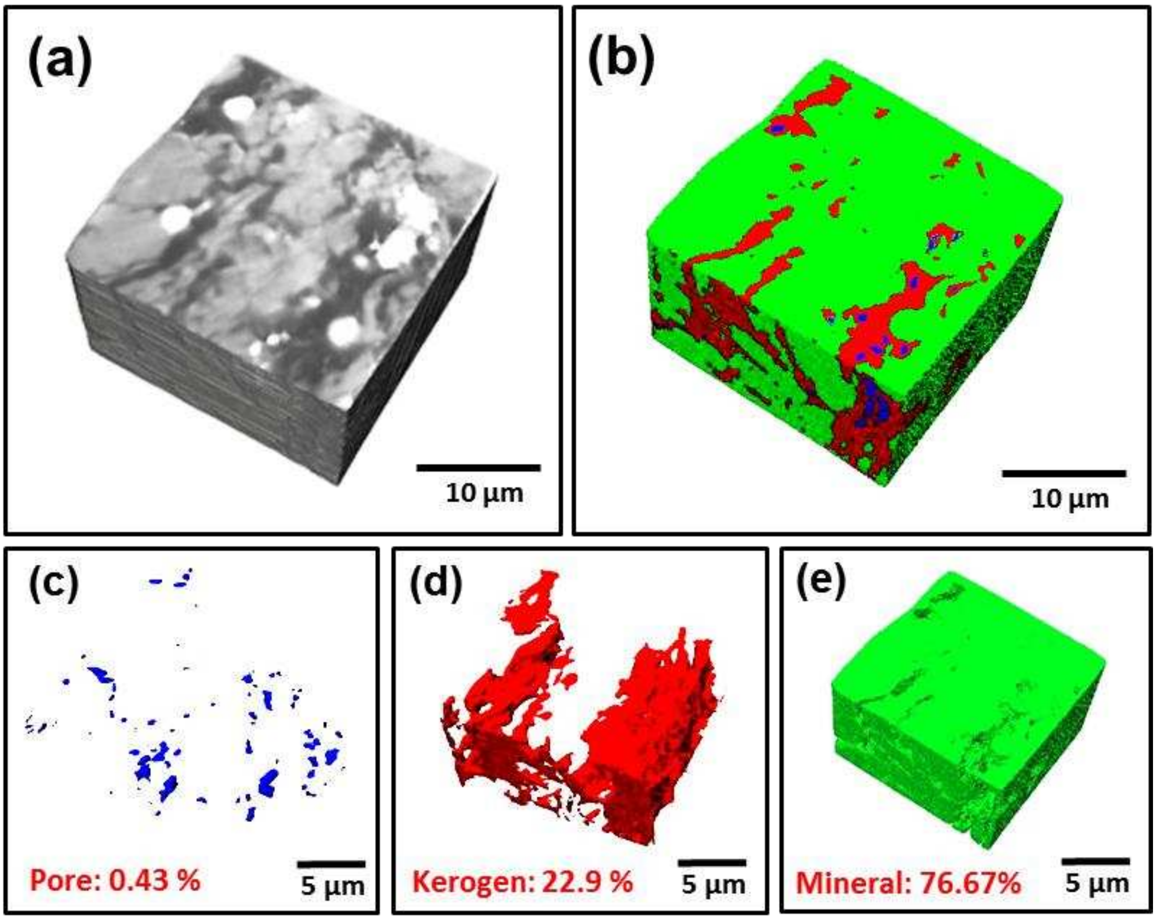

Figure 7. Nano-X-Ray Tomography (Nano-CT) for a shale rock sample with an acquired resolution of 64 nm. (a) Raw 3D grayscale image, (b) representative 3D image of all phases in the sample, (c) imaged pores, (d) imaged kerogen, and (d) solid minerals ([29]).

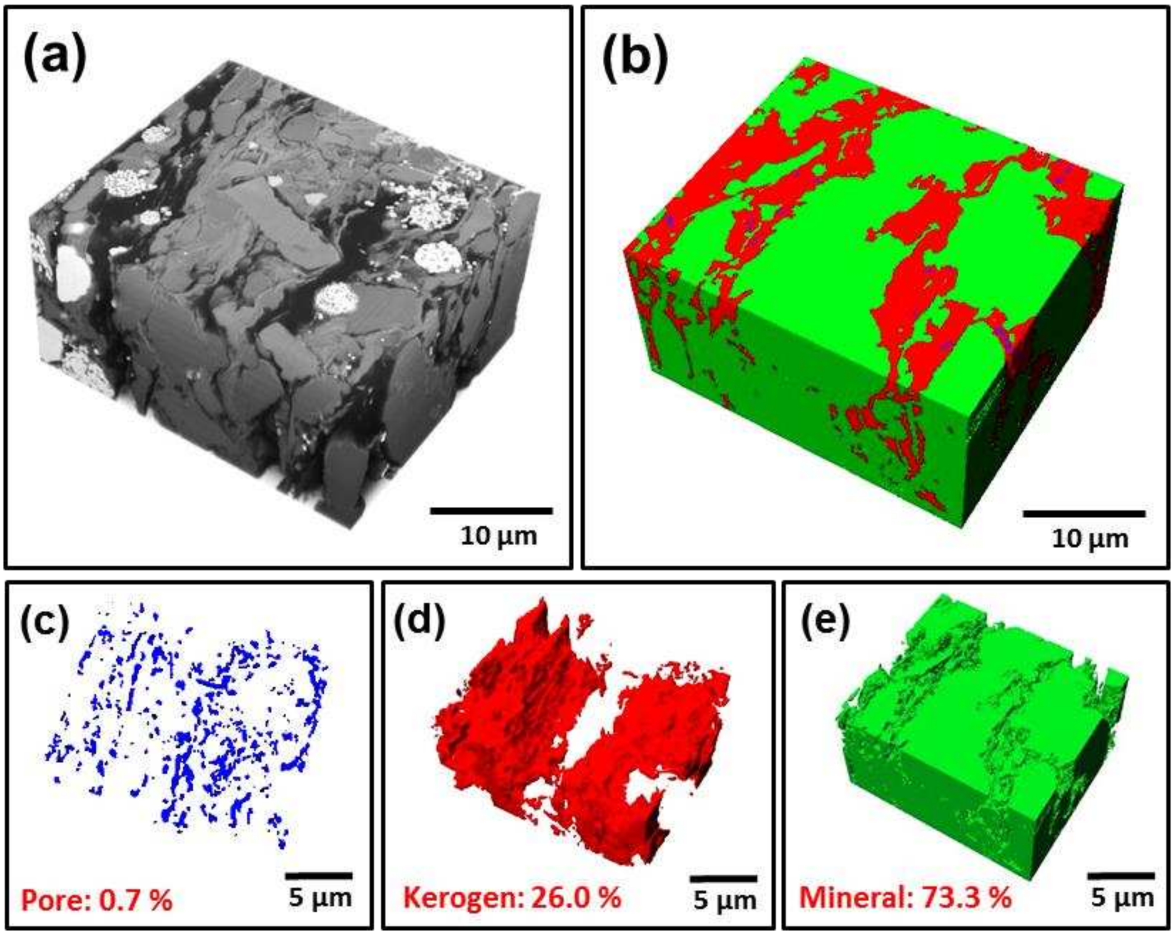

Figure 8. FIB-SEM for a shale rock sample shown at a voxel size of 0.6 µm, with an acquired resolution of 20 nm. (a) Raw 3D grayscale image, (b) representative 3D image of all phases in the sample, (c) imaged pores, (d) imaged kerogen, and (e) solid minerals ([29]).

The use of the two high resolution 3D imaging methods on the same 25 µm-sided cubic volume of rock allows us to compare the capability of the two methods in a manner which is not possible for previous studies where the measurements are made on different volumes. Figure 7a and Figure 8a provide 3D images of the same sample volume from the two techniques. The FIB-SEM measurements benefit clearly from their slightly better resolution, giving a sharper and better contrast of the resulting images. The higher resolution of the FIB-SEM technique has resulted in significantly higher measurements of porosity and slightly higher values of kerogen fraction. The larger effect on the estimation of porosity arises because the majority of the porosity is composed of a myriad of pores occurring at the limits of resolution of the two techniques. In this case, a slightly better resolution of the FIB-SEM method allows the imaging of many small pores which were just too small to be imaged by the Nano-CT resolution. This is most clearly observed by comparing the size and number of imaged pores for each technique in Figure 7c and Figure 8c.

3.2 Pore volume and size distribution

The segmented 3D data volumes were subjected to 3D image analysis to obtain porosity, the relative frequency distribution of the pore volume, the pore aspect ratios and the scale-independent pore surface area to volume ratio. These parameters were compared for both methods and for the same volume of sample. Figure 9 shows the pore-volume distribution as measured by each of the techniques. The two techniques show remarkably similar results, with the majority of the pores having pore volumes less than 0.05 μm^3. However the Nano-CT technique images have fewer of the smallest pores as a result of its lower resolution than FIB-SEM. These results suggest that the Nano-CT and FIB-SEM results are not very different in terms of the pore volume, and they both recognise the prevalence of nanoscale pores in this shale sample. However, the higher resolution of the FIB-SEM allows more of the very small pores which are too small for the Nano-CT technique to be taken into account suggesting strongly that further sub-resolution porosity in shales will be found with the appropriate imaging tool.

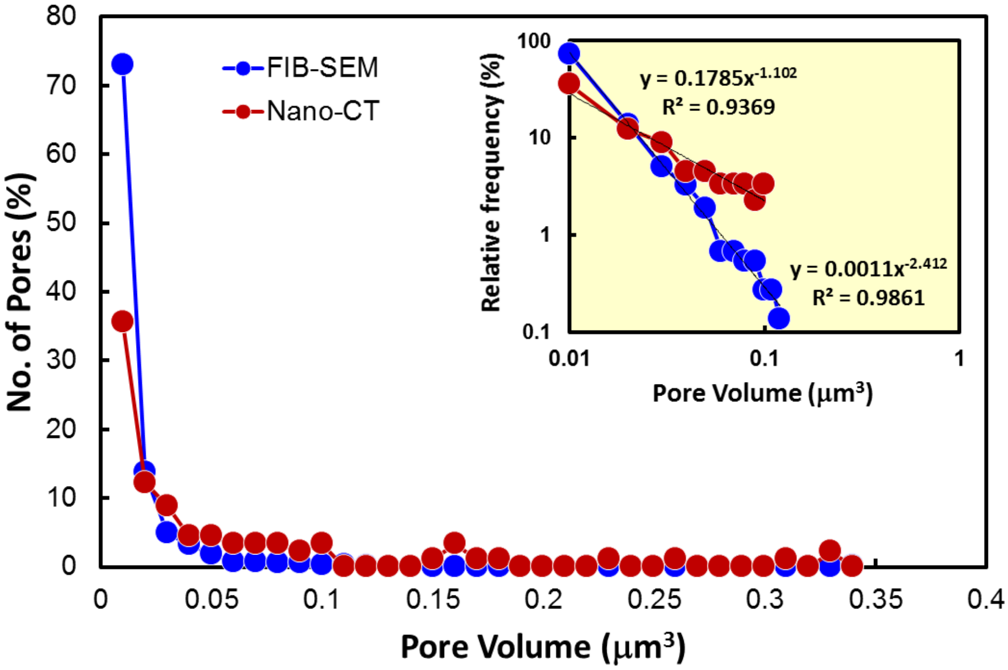

Figure 9. Normalised pore volume distribution calculated from the Nano-CT (red) and FIB-SEM (blue) 3D imaging datasets for the same measured volume of gas shale sample using 3D image analysis implemented in Avizo® Fire 9.40 software. The inset shows the low pore volume data on an expanded scale.

The data shown in Figure 9 show well developed negative linear trends, which fit the power law distributions y=0.0011x-2.41 and y=0.1785x-1.102 and R^2 values of 0.9861 and 0.9369, for FIB-SEM and Nano-CT, both respectively. In each case the fit was based on those data in the set which ranged from the lowest pore volume not affected by resolution thresholding to that just above the first 0% relative frequency in order that the power law fit could be carried out. Consequently, in this way, we are able to infer that there may exist a large number of pores smaller than the resolution of the technique.

Figure 10 shows a comparison of the pore size distribution obtained using the MIP, FIB-SEM and Nano-CT methods. In terms of the distribution by pore count (Figure 10a), the FIB-SEM provides slightly lower values of equivalent pore diameter (approximately 100-500 nm). This distribution does not peak at the resolution of the technique, which as we shall later see is due to the failure of the equivalent pore diameter to accurately describe the pores in shales. The distribution for the Nano-CT method peaks at 300 nm, and it is expected that the decrease for smaller values is related to the resolution of the Nano-CT measurement. If the distribution is plotted on the basis of the pore volume represented by each equivalent pore size bin, a different distribution might be obtained than when using other methods. For the Nano-CT data, it is clear that the very few pores with equivalent pore volumes greater than 1000 nm (1 μm) according to Figure 10a have a disproportionate significance in terms of pore volume (*cf*. Figure 10b).

We attribute the curtailment of the data for both the FIB-SEM and Nano-CT to the underlying assumption in this equivalent pore diameter figure that all pores are spherical. As we shall see later, the pores in this shale sample are very elongated, allowing the size of at least one pore dimension to be affected by resolution issues and still provide a pore volume that gives a higher equivalent pore diameter.

Mercury injection porosimetry was also carried out on a sample of rock taken from close to where the imaging samples were taken in the same core plug. The MIP data does not provide data by individual pore count, but by intruded volume, and consequently, is given only in Figure 10b. The range of values for pore size from MIP is 3 nm to 700 nm. The MIP measurements indicate that it is possible, and indeed likely, that there exist pores of dimensions lower than those measured due to the limitations of the resolution. However, other techniques with higher resolution exist and able to resolve pores at 1 nm, such as (N_2/CO_2 adsorption) [41, 42, 43 and 44]. Such measurements to be made and will be reported in a further paper.

The mercury intrusion (MIP) approach measures pore volume at a given pressure corresponding to the pore throats permeable to mercury at this pressure and which are connected to the mercury percolation cluster. Consequently, unlike the imaging data, the x-axis MIP data must be interpreted as the diameter at which mercury passes through small pore throats to fill larger pores, while the y-axis value represents the volume of those larger pores filled through the small pore throats. Hence the apparent large volume of very small pores shown by the MIP technique in Figure 10b is not likely to be the case in reality, with the volumes shown being present in larger pores that can only be accessed by the mercury through smaller pore throats. The interpretation of the MIP should also be carried out with due regard to the compaction and fracturing problems associated with using the MIP technique on shale rocks that were mentioned earlier.

Furthermore, the pore diameter from MIP refers only to the connected pores, this is because mercury is introduced to the pore spaces through connected paths under increasing pressures up to 60,000 psi corresponding to a pore throat of 3 nm (Figure 10). Consequently, the pore size distribution and porosity measured by MIP on the bulk rock sample is restricted to accessible or connected pore spaces. By contrast, both imaging methods include both connected and isolated pores.

For the purposes of Figure 10, the pore size for the imaging methods (Nano-CT and FIB-SEM) is the equivalent pore diameter d_{Eq}, which was taken to be the diameter of a sphere with the same pore volume, hence [45]:

$$d_{Eq} = \left(\frac{6V}{\pi}\right)^{1/3} \quad \textbf{(1)}$$

Results given later in this work and in other studies indicate that the assumption of spherical pores for the great majority of pores in shales is incorrect, but we give it here as a reference point. Since most pores in shales are oblate, it is misleading to use a single pore diameter.

Different scales methods available for pore diameter and the characteristics of the shale rock resulting distributions have been used previously in the literature (e.g., 15, 37, and 46). Each of these have their own advantages as well as limitations.

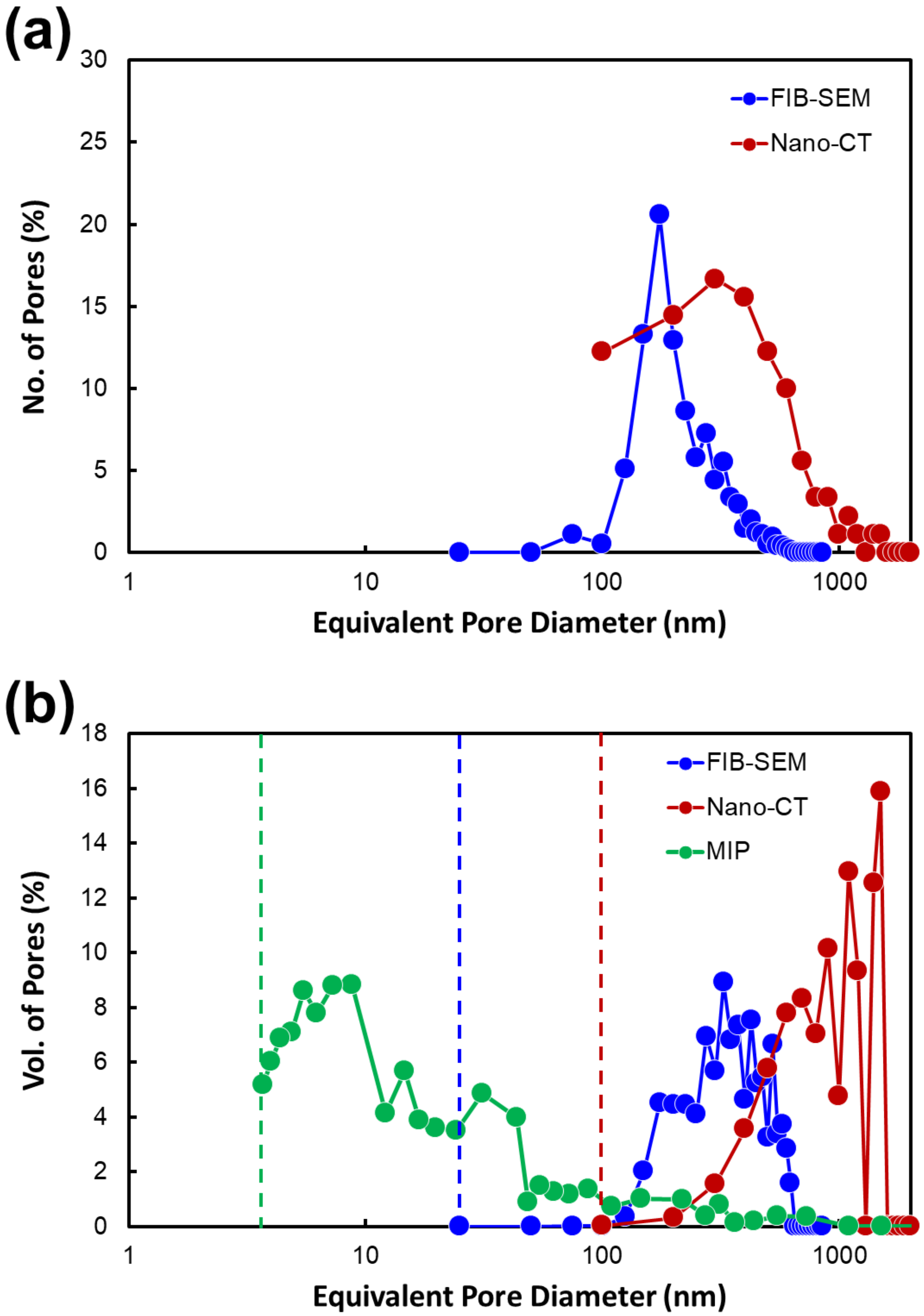

Figure 10. (a) Pore number, and (b) pore volume distributions of the equivalent pore size (assuming spherical pores) calculated from the Nano-CT (red) and the FIB-SEM (blue) 3D imaging datasets for the same measured volume of gas shale sample using 3D image analysis implemented in Avizo® Fire 9.40 software. The MIP measurements (green) were made on a sample from the same core plug. Dashed lines show native resolution limits for each technique.

Porosities of 0.43% and 0.7% were obtained from the Nano-CT and the FIB-SEM approaches, respectively (Table 2). The two measurements are made on exactly the same volume of sample. The MIP measurement was made on a sample that was cut from the same shale core and gave a porosity of 1.8%. The disparity in the results may be caused by a number of effects. The small disparity between the two imaging approaches probably arises from the FIB-SEM's higher resolution taking account of a large number of small pores which are below the resolution of the nano-CT approach. The larger difference between the imaging and MIP porosities may be caused by (i) the different resolution within measurements naturally having a different porosity, such as the MIP resolution can only resolved smaller pore at approximately (3.6 nm), thus will give a larger porosity [47] (ii) the sample preparation and measurement of the MIP technique inducing porosity in the samples in the form of micro-fractures, and (iii) the larger sample size of the MIP sample (approximately 5 mm in each dimension, compared to 25 μm for the imaging techniques) allowing a small number of large pore to skew the porosity measurement, either erroneously or by including representative pores which the small 3D fields of view of the imaging techniques take no account of. It should also be remembered that the MIP approach only measures connected porosity, while the imaging techniques measure all porosity (within resolution limits). It should note, sometimes the pore connectivity is overestimated by the 3D imaging methods because at the limits of their resolution they may consider a number of disconnected smaller pores as one larger pore [48].

3.3 Pore aspect ratio distributions

Aspect ratios are measures of the shape of a pore by comparing two characteristic dimensions, often the largest to the smallest, such as the length of a crack to its aperture [27]. Void spaces (and grains) within the rock may be generalised by assuming that they conform to an ellipsoidal shape, with half-lengths in each of three mutually perpendicular directions being labelled a, b and c. Ratios of each pair of these define an aspect ratio, although any two aspect ratios are sufficient to define the system fully.

We have chosen to use two pore aspect ratios. The first is given by $S = c/b$ (Figure 11a-b), where b is the maximum dimension of the pore, and c is the minimum dimension of the pore. The second aspect ratio is given by $L = a/c$ (Figure 11c-d), where a is the half-length of the pore mutually perpendicular to both b and c.

The pore aspect ratios are measures of the shape of the pore. If the pore is equant (approaching spherical) then $S \approx L \approx 1$. If the pore is penny–shaped (flattening or elongation), then $S << 1$ and $L > 1$. If the pore is pin–shaped (prolate), then $S << 1$ and $L \approx 1$. The value of both pore aspect ratios is important because pores which are long and thin ($S \ll 1$) or have a significant sideways extent ($L \neq 1$) have a greater potential for connecting up with other pores, contributing to raising the chances that the pore structure forms an interconnected network which will support gas flow.

Figure 11 shows the distribution of the number and volume of pores as a function of the pore aspect ratios, for all data estimated from both the FIB-SEM and Nano-CT methods. It is immediately clear that both aspect ratios differ from unity, indicating that all pores measured by both imaging methods are significantly non-spherical, but better resemble oblate (penny shaped) pores.

Parts (a) and (b) of Figure 11 show the S aspect ratio distribution in terms of number and volume, respectively. In both of these a value approaching unity indicates a more equant pore shape. The range of S obtained from nano-scale pores measured by the FIB-SEM method are between 0.025 to 0.65 (Figure 11a). By contrast, the range of values of S obtained from the Nano-CT technique are between 0.025 to 0.7. There is remarkable similarity in the range of S aspect ratios given that the data from which they are derived were measured by very different techniques. Both techniques show the preferred range of S-values occurs between 0.2 and 0.45, which corresponds to pores between 2.22 and 5 times their aperture. However, the fine structure in the two distributions is different, with major peaks in the Nano-CT occurring at 0.26±0.08 and 0.4±0.05, while the minor peak in the FIB-SEM results occurs at 0.3±0.04. Importantly, however, all of these values are significantly less than unity, with the lowest values (0.025) indicating that the pores are up to 40 times longer than they are wide (Figure 11a).

While Figure 11a indicates the pore number distribution of the S aspect ratio concerned, transport through pores may be more sensitive to the volume of each of the pores rather than their number. In other words, a large number of pores of a given aspect ratio may be inconsequential compared to a smaller number of pores with a larger volume. Figure 11b shows the pore volume distribution of the S aspect ratio. The pore volume is distributed in pores which have S pore aspect ratios significantly less than unity, and are unimodal for each technique, with peaks at 0.25±0.08 and 0.1±0.05 for Nano-CT and FIB-SEM, respectively. This indicates that the most significant proportion of the pore volume occurs in the shape of pores which are about 4 or 10 times longer than their aperture according to the measurement method. The FIB-SEM data has a tendency towards the smaller values because it has the extra resolution that allows it to resolve pores which are very thin and which will be more likely to have very small S aspect ratio, compared to the nano-CT method, which would miss these pores.

Comparing parts (a) and (b) of Figure 11, it can be seen that the same value of the aspect ratio (say, 0.25) can have very different percentage number of pore and percentage pore volume. For example, according to the Nano-CT measurements, for $S = 0.25$, 10% of the pores by number represents about 24% of pore volume, indicating that, on average, pores with this value of S are larger, while for $S = 0.4$, 13.5% of the pores by number represents about 5% of pore volume, indicating that pores with this value of S are smaller.

While the S aspect ratio distinguishes the extent to which the pore's greatest extent exceeds its extent in the other dimensions, it does not distinguish whether these long pores are penny-shaped or needle shaped. The L aspect ratio data shown in parts (c) and (d) of Figure 11 can be used to make this distinction. A value of L approaching unity indicates a pore where the two shorter axes are approximately equal, resulting in a needle-like or prolate pore. When $L > 1$, the two shorter axes diverge, leading to a more flattened pore shape, until the limit where $L=1/S$, which occurs when the pore is fully penny-shaped.

Figure 11c shows the pore number distribution of L aspect ratio values acquired from the FIB-SEM and Nano-CT methods. The range value of L obtained from FIB-SEM data lies between 1 to 2, while, the range of values of L obtained from the Nano-CT technique is similar, lying mainly in the range 1 to 1.9. Importantly, however, the both data sets clearly show that the value of the L aspect ratio is only slightly greater than unity, indicating that the pores are predominantly needle-shaped. The pore volume distribution of L aspect ratio values (Figure 11d) shows a similar distribution for that of pore number, indicating that both the number and volume of the majority of pores has its two shorter axes about equal, with their form approximating to a needle-shape.

Different shales will exhibit different aspect ratios, implying differences in pore connectivity and consequently in their gas permeabilities. Shales which have lower values of S and higher values of L should offer the greatest permeability on the basis that it is more likely for these long flat pores (crack-like pores) to intersect and form a connected pathway for fluid flow. Our results suggest that the aspect ratios of pores in shale sample A are of the type which are more likely to lead to connected pore networks. Our results also show that the same conclusion is reached irrespective of whether we use Nano-CT or FIB-SEM data because these two datasets are broadly in agreement.

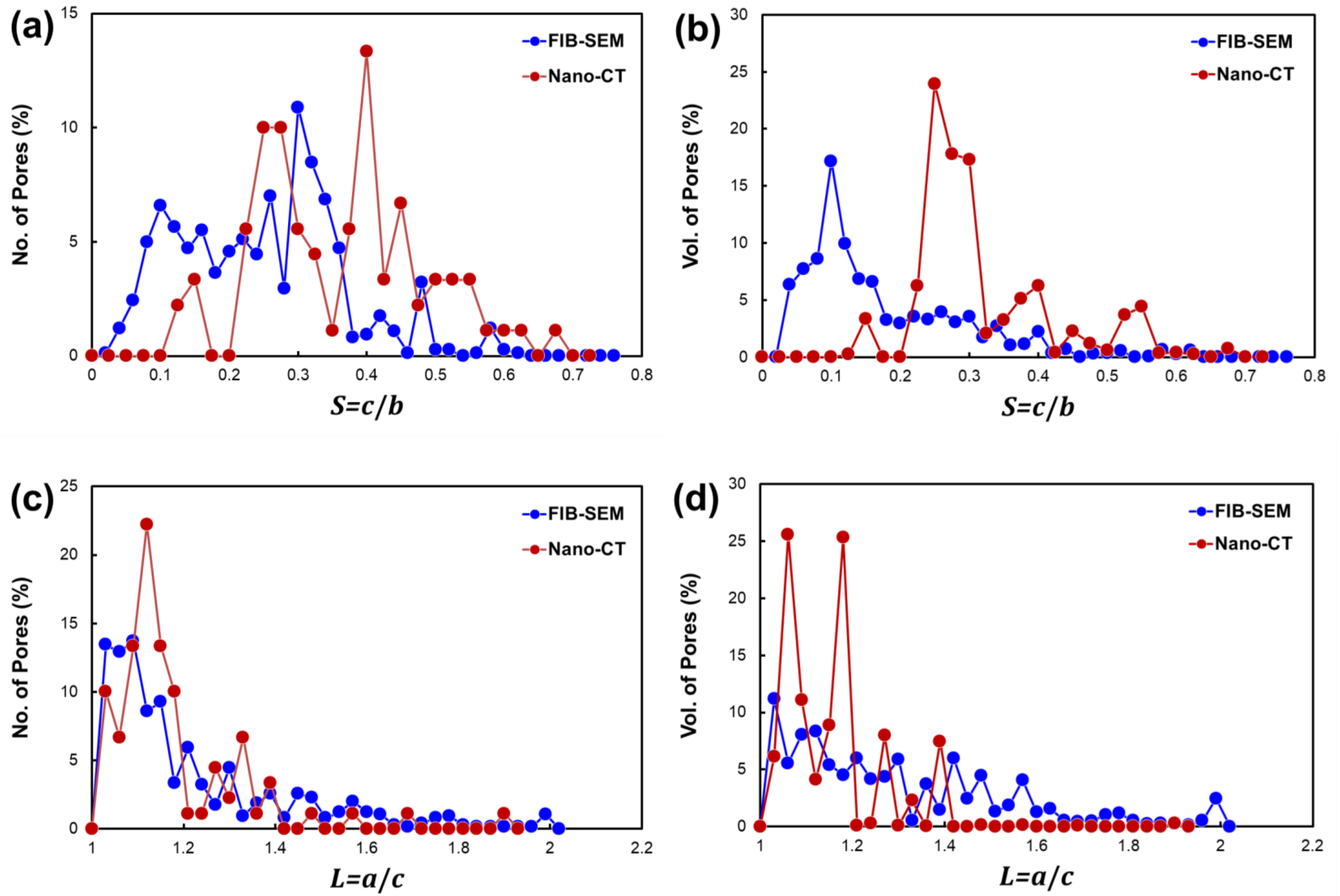

Figure 11. The pore-aspect ratio distribution, plotting the overall number of pores expressed as a percentage of the total number of pores in the sample for (a) the S aspect ratio, and (c) the L aspect ratio. The pore aspect ratio as a function of total volume of pores for (b) the S aspect ratio, and (d) the L aspect ratio. In each case data is derived from 3D imaging of the same volume of gas shale sample A using both FIB-SEM and Nano-CT techniques.

3.4 Pore surface area to volume ratio

The pore surface area to volume ratio ξ [27] is another indicator of pore shape. A spherical pore represents the most efficient use of surface area to contain a given volume, while higher values of surface area to volume ratio indicate the presence of a larger surface area per unit volume of pore space, which occurs as the pore shape changes from that of a perfect sphere, particularly if the pore becomes oblate (penny-shaped).

The shape of the pores can be significant in shale gas reservoirs in a number of ways. For example, pores that are more spherical represent an efficient volume for the storage of gas. These spherical pores are also much less likely to collapse under externally applied pressure than crack-like or linear pores, which tend to close easily when subjected to even a small normal stress [8]. Consequently, sub-horizontal crack-like pores observed in samples at surface pressures are very unlikely to remain open at reservoir depths. However, long, thin pores, with high surface area to volume ratios are more likely to interact with other pores and cracks, making them much more effective at increasing pore connectivity and leading to higher permeability [49]. Perhaps most importantly, large surface areas facilitate the diffusion of gas initially trapped in the matrix of the rock and in the kerogen into the pore spaces within the shale [49]. This is an essential stage before hydraulic fracturing of the shale rock can open up access to these small pore spaces. A high surface area thus ensures that the diffusion procedure is more efficient, not only ensuring a good initial charge of gas in the micro-pores of the shale, but also allowing those pores to be recharged quickly once initial production has removed the initially accumulated gas.

Generally, flat pore shapes have high values of surface area to volume ratio [27]. However, simple surface area to volume ratios are scale-dependent (their dimensions are per length), which results in smaller pores generating higher values of surface area to volume ratio than larger pores of the same shape. The scale dependence makes the use of a simple pore surface area to volume ratio ξ invalid for comparing pore shapes at different scales. Consequently, , we have introduced a parameter in a previous paper [27], which we name the Scale-Invariant Surface Area to Volume Ratio, presented by σ, to avoid any inconsistencies, and it is defined as

$$\sigma \equiv a\,\xi, \quad \textbf{(2)}$$

Where a is the half-length of the intermediate dimension of the ellipsoid. The value σ, as its name suggests, is independent of scale and is only sensitive to the shape of the pore. Hence, it may be used to judge how shape changes with pore size pore.

Spherical pores have σ=3. As one axis becomes longer (b in our protocol) the value of σ becomes larger, reaching σ=15.45 when the long axis is ten times the smallest half-length (i.e., b=10c) and σ=150.08 when b=100c. It is an interesting observation that the use of the intermediate half-length (a in this paper) as the scaling length in Equation (2) results in these values remaining the same, irrespective of the value of a with respect to the other half-length values. Consequently, the scale invariant surface area to volume, when defined in this way is equally valid for oblate or prolate pores.

Figure 12 shows the distributions of the percentage number and volume of pores as a function of σ, measured by both Nano-CT and FIB-SEM techniques. Considering the pore number distribution (Figure 12a), it should be noted that the values obtained from both Nano-CT and FIB-SEM measurements are always greater than 3, as demanded by the mathematical model. However, there are peaks in both distributions close to 3, indicating that many pores approach sphericity. We hypothesise that these pores are those at such a small scale that they are under-represented in the datasets. However, in the data for both techniques there are a significant number of pores which exhibit σ values up to about 10, gradually decreasing for the FIB-SEM data and clustered at about σ=6.0±1.5 for the Nano-CT data. These values indicate that there is a tendency away from sphericity for many of the pores in a manner that is consistent with parts (a) and (c) of Figure 11.

Considering the pore volume distribution (Figure 12b), the signal for values as σ approaches 3 is much reduced for the FIB-SEM data and almost to zero for the Nano-CT data, consistent with our previous hypothesis. For this figure, the peak in the pore volume occurs at 4.0±1.6 and 7.5±2.0 for the FIB-SEM and Nano-CT data, respectively. This indicates that the pores which contribute more to the pore volume tend to be those that diverge more from sphericity (and using the aspect ratio data are known to be needle-shaped).

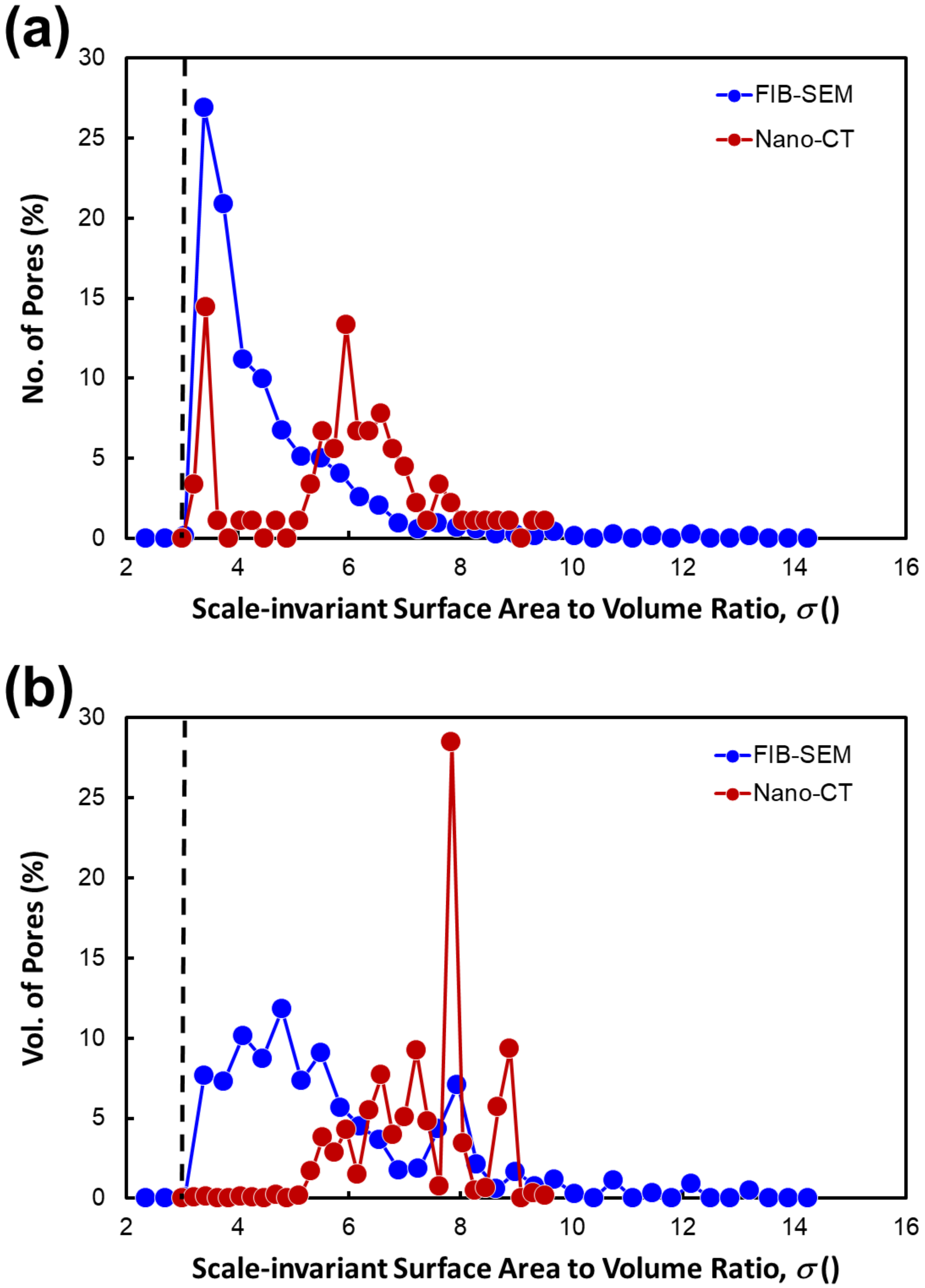

Figure 12. The scale-invariant pore surface area to volume σ distributions with respect to (a) percentage number of pores and (b) percentage pore volume, each calculated from 3D imaging of the same volume of gas shale sample A using both FIB-SEM and Nano-CT techniques.

4. Gas Transport Simulation in Kerogen

Gas transport through shale reservoirs is very complex due to (i) the very small size of pores, (ii) the limited connectivity of pores, and (iii) the presence of multiple physical and chemical processes which both aid and hinder gas transport and which occur at different scales [42]. In order to describe the gas transport simulation in the shale, a simulation must be provided with at least one connected path across the whole area of interest. In our case, the pores were unconnected and therefore we simulated the flow through the kerogen as well as the pore system. This approach follows similar modelling and simulation carried out by a number of other researchers [45, 51,52,53,54, 55 and 56] but these dynamics are not considered in the current permeability simulation process.

As connectivity was found within the kerogen network in the image sets, the volumes of interest with a local connected system were selected (Figure 7d and 8d) for simulation and comparison. Experimental data for associated samples of this rock indicates that the shale does have a measurable permeability at a larger scale and therefore selecting a sub-sample to calculate the permeability is a reasonable approach although it does reduce the representativeness of the results. The results for the permeability along the *x*-, *y*- and *z*-axis respectively are presented in Table 3.

Figure 13a shows the FIB-SEM images which have been used in this study for simulation within the kerogen (white arrows) as can be seen, while Figure 13b shows a diagram of gas molecules (yellow spots) flow through the kerogen.

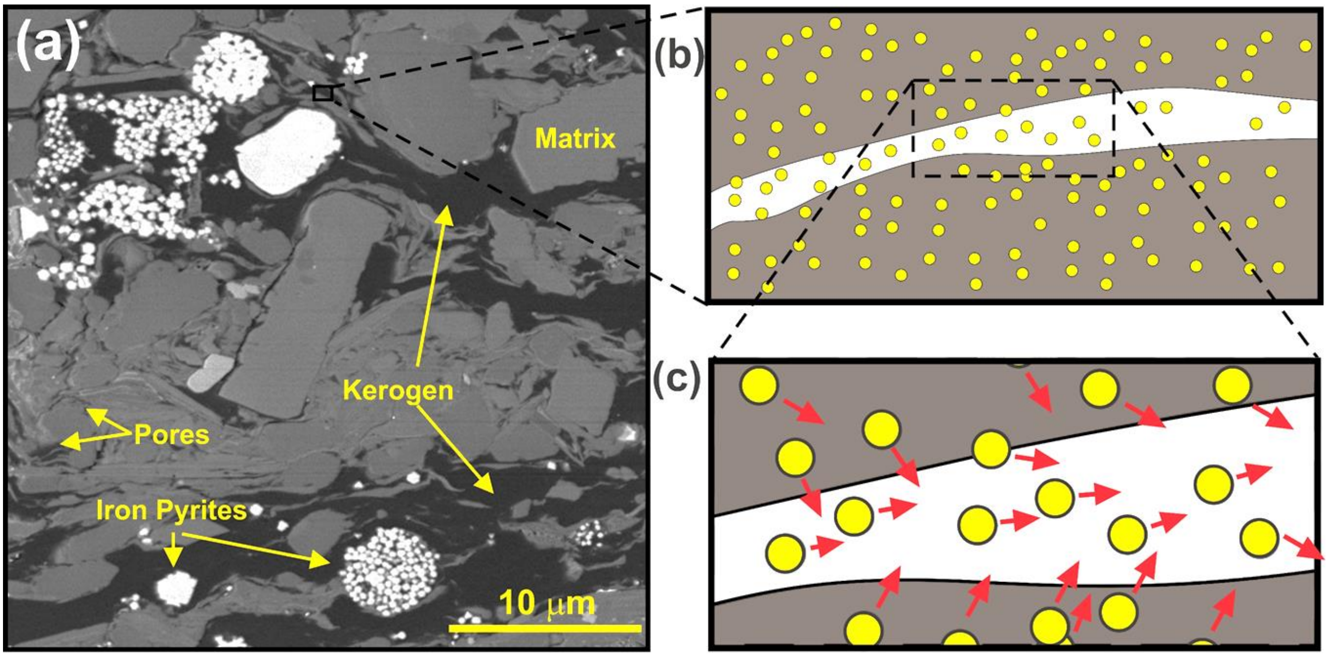

Figure 13. (a) FIB-SEM image revealing kerogen (darkest areas) with some of pyrite (lightest areas) in a matrix of medium greys with a few small pores (black). (b) Gas flow in the kerogen (textured brown), the yellow dots represent gas molecules which can flow and accumulate within the kerogen, and the white areas represent pores.

The segmented volumes from the Nano-CT and FIB-SEM images were used to calculate the permeability of the shale using a pore-scale finite volume solver that combines Darcy flow and Stokes flow into a single elliptic flow equation [57]. This method is an extension of flow-based permeability upscaling [58, 59] to include pore space explicitly.

For simplicity we assume single phase incompressible laminar flow [60] and the flow is assumed to be purely advective [61]. We recognise that this is a gross oversimplification of the physical processes, but limitations caused by the software we use and the data we have available makes it necessary.

We ignore the effects of gas slippage (Klinkenberg effect) which become significant when the mean free path of molecules becomes comparable with the channel dimension and thus, we are calculating the high pressure or liquid permeability [62]. The effects of gas slippage typically increase the permeability at low pressures. However, we also ignore the effect of absorbed gas molecules on the surfaces of pores which is known to decrease shale permeability at high pressure [62].

Each voxel is assigned an effective conductivity, g, which relates the volumetric flow rate, $\vec{q}$, to the pressure gradient:

$$\vec{q} = -g\nabla P. \tag{3}$$

Mineral voxels are assumed to be non-conducting. Kerogen voxels use Darcy flow where the connectivity is proportional to the permeability and pore voxels utilise Stokes flow using a Finite-Difference Geometrical Pore Approximation (FDGPA) method [63]. In the FDGPA method, the connectivity of each pore voxel is a function of two variables: the Euclidean distance of the voxel to the pore wall, d, and the local maximum of the Euclidean distance, d_{max}. The connectivity of kerogen and pore voxels are calculated as follows [64]:

$$g = \begin{cases} \frac{kA}{\mu}, & \text{in kerogen voxels} \\ \frac{A}{8\mu}(2dd_{max} - d^2), & \text{in pore voxels} \end{cases}, \tag{4}$$

Where μ is the fluid viscosity and A is the cross-sectional area of the voxel perpendicular to the direction of flow and k is the kerogen permeability.

For the kerogen, a constant effective permeability k of 2.55 nD and 9.92 nD was obtained from the Nano-CT and FIB-SEM data, respectively. These values are estimated from the equation: [49].

$$k = \Lambda^2/8F, \tag{5}$$

Where Λ is a value measure of the aperture for fluid flow which controls the permeability in the sample, and F is the formation factor of the rock [49].

The value of Λ was obtained from the surface area to volume ratio of the kerogen following the approach of Johnson et al. [65], where,

$$\Lambda = S_p/V_p, \tag{6}$$

The formation factor of the rock was not measured directly in this work. Instead, it was estimated using

$$F = \chi_k^{-m}, \tag{7}$$

Where χ_k is the kerogen phase fraction and m is the phase exponent from the generalised Archie's law [66, 67]. For this work we have assumed that m=3. This value was chosen since the cementation exponent for shales is known to vary between about 2.34 and 4.17 [68]. The calculated shale permeability in x, y and z directions from simulation (Figure 14) for Nano-CT and FIB-SEM images is given in Table 3.

The FDGPA method essentially uses an analytical solution of the Stokes equation which is exact for cylindrical pore throats but is less accurate for pores with highly elongated cross-sections [63]. In our case, the fraction of pore voxels is small and therefore the overall error due to the approximation in the FDGPA method should be small.

The conservation of mass can be expressed as

$$\nabla \cdot \vec{q} = 0, \tag{8}$$

Which leads to a generalised Laplace equation,

$$\nabla \cdot (g \nabla P) = 0. \tag{9}$$

Two opposite faces of the model are designated; the inlet and outlet, with arbitrary constant pressures differing by ΔP. The other four faces of the model are no-flow boundaries. The generalised Laplace equation is discretised in the voxel model using a two-point flux approximation leading to a system of simultaneous linear equations where the unknowns are pressures in each voxel. Mineral voxels are removed from the calculation (since they are assumed to be non-conducting) and the system of equations obtained is solved using a conjugate gradient algorithm with an incomplete Cholesky factorisation pre-conditioner [64]. The total inlet (or outlet) flux, Q_T, is calculated and the permeability follows from Darcy's law,

$$k = \frac{Q_T \mu L_T}{A_T \Delta P}, \tag{10}$$

Where L_T is the length of the model in the direction of flow and A_T is the cross-sectional area of the model perpendicular to the direction of flow.

The permeability was measured in the laboratory on an associated sample using the GRI method (see Section 2.5).

Table 3. The calculated permeabilities in the x, y and z directions obtained from simulation for Nano-CT and FIB-SEM, using Equation (5) and measured in the laboratory.

	Permeability from flow simulations		Permeability calculated with Eq. (5)		Permeability measured in the laboratory
	Nano-CT	**FIB-SEM**	**Nano-CT**	**FIB-SEM**	
	k (nD)	k (nD)	k (nD)	k (nD)	k (nD)
x-axis	0.003	0.006	2.55	9.92	1.74±0.65
y-axis	0.180	1.43			
z-axis	0.321	1.66			

It is striking that the permeability results lie close to each other, in the low nano-darcy range, despite arising from different experimental and simulation techniques and based-upon different imaging datasets made using different imaging approaches. This is remarkable given the experimental and simulation difficulties encountered in measuring and calculating such small permeabilities. However, the differences in scales of measurement should be noted. The calculated permeability from flow simulation relates to a scale of around 25 µm whereas the laboratory measured permeability relates to a considerably larger scale of circa 1 mm. The differences in gas pressure may also be significant. The calculated permeability relates to high pressure where gas slippage is negligible whereas the laboratory measured permeability can be obtained depends on the pressure recorded and experimental volumes (crushed particles size of shale). Irrespective of the apparent good correlation between the modelled and measured permeabilities, it is worthwhile noting that (i) the comparison is only for one sample, which cannot be considered to be statistically reliable, (ii) there are significant simplifying assumptions in the modelling, including the assumption of incompressibility, and (iii) there might be errors in the experimental measurements.

The simulated permeability components are dominated by the amount and spatial distribution of the kerogen. The simulated permeability is also strongly dependent on the assumed permeability of kerogen, as discussed above. Since the imaged datasets contained no connected kerogen in the x-direction, the permeability in this direction is calculated to be very low for both Nano-CT and FIB-SEM approaches. The FIB-SEM image has 26% kerogen compared with 20% in the Nano-CT image, giving rise to the lower calculated permeabilities for the Nano-CT dataset in both y- and z-directions.

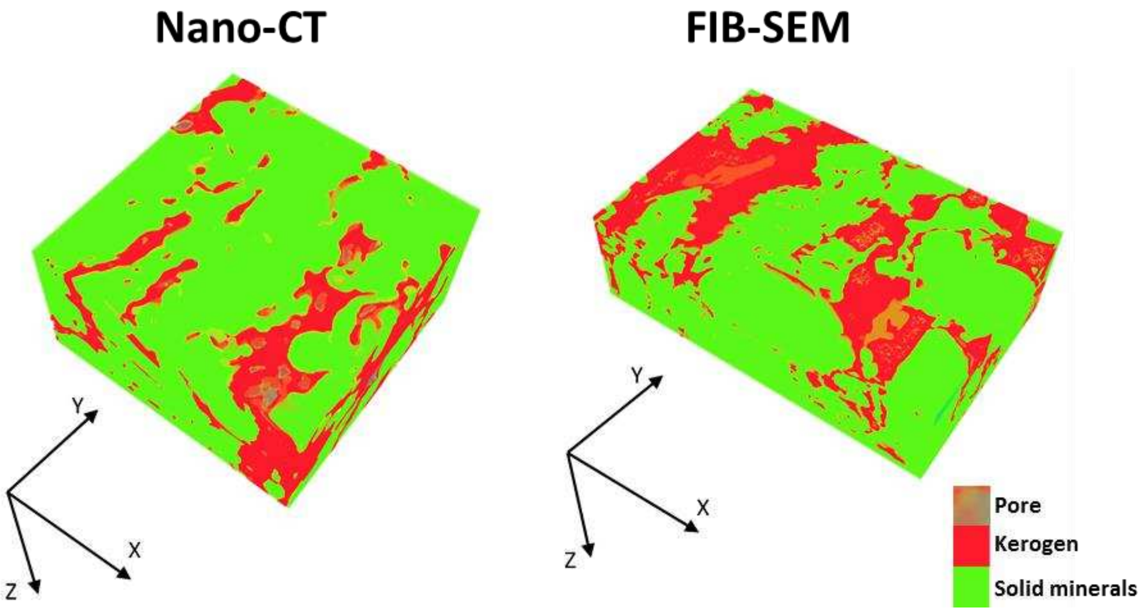

Figure 14. Shows the gas flow through kerogen (red colour) in the three directions (x, y and z) for Nano-CT and FIB-SEM.

5 Kerogen and pore connectivity

Kerogen is important in gas shales because it is the source of the hydrocarbon gas. The type, fraction and connectivity of kerogen control the chemical and physical properties of the shale, significantly affecting both the storage and flow of the hydrocarbons [69, 70]. Previous authors have identified kerogen associated with pore systems in shales, and have proposed that gas transport through kerogen might be possible [71, 72, 73].

In this work, kerogen and pores have been identified using both Nano-CT and FIB-SEM imaging. The kerogen presents a much higher percentage volume fraction than pores (Table 2). Moreover, qualitatively kerogen has a much higher connectivity than the pores, at least at scales higher than the resolution of the imaging techniques (>20 nm). This can be illustrated by comparing parts c and d of Figure 7 and Figure 8. It is possible, even likely, that pores smaller than the imaging resolution are present and are very well connected. However the extent to which this may be the case will need higher resolution imaging than we have been able to carry out. Indeed, the presence of an experimentally measureable permeability for gas in shales is an indication that connectivity is somehow much better than that observed in imaging down to 20 nm. It is interesting that the permeability calculations using Equation (8) and the simulations described previously used the kerogen phase as a gas transport medium, and provided permeabilities comparable to those measured experimentally.

The levels of pore and kerogen connectivity that we obtained in this work are very similar to the results of Ma et al. [74], and hence we consider that our measurements, albeit on a single sample, are not significantly atypical. Consequently, we may hypothesise that (i) there is a significant pore volume consisting of pores too small to have been currently measured, which are sufficiently well-connected to provide the permeabilities obtained experimentally, or (ii) gas transport through the kerogen is more prevalent than previously expected, or (iii) a mixture of both.

It has been also noted that, in FIB-SEM images, pores were observed to be locally connected in the sample, and some of them are connected to other pores in the matrix (Figure 8c). The majority of pores in this sample are isolated at this scale. These locally connected pores were also observed in the studies of [27, 75, and 76].

6 Conclusions

In this paper, we have used two high resolution 3D imaging techniques (Nano-CT and FIB-SEM) to investigate the pore structure and kerogen structure of the same 25 μm-sized volume of a sample of gas shale for the first time. It is increasingly common to carry out either Nano-CT or FIB-SEM imaging on rock samples, but rare to carry out both techniques, and when this is done, authors typically use different samples or different imaged volumes in the same sample. To our knowledge, this is the first time that the two techniques have been applied to the same 25 μm-sided cube of rock, thus allowing a direct comparison of the two measurement techniques to be made.

The two resulting 3D datasets have each been used to calculate a range of micropetrophysical parameters describing the volume and distribution of the pores and kerogen in the sample. These parameters include pore and kerogen volume and size distributions, pore aspect ratios and scale-invariant surface area to volume ratios.

Both imaging techniques provide 3D images that are clearly of the same sample volume. The FIB-SEM measurements benefit clearly from their slightly better resolution in the sharpness and contrast of the resulting images. The higher resolution of the FIB-SEM technique has resulted in significantly higher measurements of porosity and slightly higher values of kerogen fraction because the extra resolution. The larger effect on the estimation of porosity arises because the majority of the porosity is composed of a myriad of pores occurring at the limits of resolution of the two techniques.

Sample A was found to be composed of different amounts of pores, kerogen, silicate matrix and iron pyrites by both methods. The porosities and kerogen fractions were found to be 0.7%, 26.0% for FIB-SEM, and 0.43%, 19.6% for Nano-CT, respectively. Overall, the pore volume observed by Nano-CT ranged between 0.017 to 0.35 μm^3, while the corresponding range for FIB-SEM analysis was between 0.009 and 0.33 μm^3.

A critical finding was that for both imaging methods the pores showed very little connectivity and no evidence for the gas transport pathways that the experimental pulse-decay permeability measurements imply.

This study also opens a new path in the better understanding of the level of the connectivity of pore and kerogen involved in transport not only in shale rock samples but also in other nanoporous materials. The novel technique that has been applied in this study can be easily extended to other nanoporous materials used in medical applications, food industry, and catalytic reactions, as well as nano-membranes and fuel cells.

The measurements have been used to calculate the permeability in each Cartesian direction using a Finite-Difference Geometrical Pore Approximation (FDGPA) method, and also using an analytical equation. These calculations both made the assumption that gas flow occurs through the kerogen. There was good agreement between the permeabilities obtained with both of these methods and the permeability measured experimentally using a pulse-decay method.

We hypothesise that the experimentally determined permeabilities can only be obtained if there is significant highly connected pore volume at a sub-resolution scale, or gas transport through the kerogen is more prevalent than previously expected, or a mixture of both.

7 Acknowledgments

The authors would like to thank the Leeds University Electron Microscopy and Spectroscopy Centre (LEMAS) for technical support (Stuart Micklethwaite), with special thanks to Mr John Wynn Williams of Leeds University School of Earth and Environment for sample preparation, and also would like to thank to Henry Royce Institute in particular David Stanley through the Royce Equipment Access Scheme enabling access to X-ray facilities at Royce@ Manchester; EPSRC Grant Number EP/19/0044, and Anne-Marie Clift from Armourers and Brasiers for their financial support.

References

1. Hefley, W. E. & Wang, Y. 2016. Economics of unconventional shale gas development, Springer.
2. Bustin, R.M., Bustin, A.M.M., Cui, A., Ross, D., Pathi, V.M. 2008. Impact of shale properties on pore structure and storage characteristics. Paper SPE-119892-MS.
3. Washburn, K.E., Birdwell, J.E., Foster, M. and Gutierrez, F., 2015. Detailed description of oil shale organic and mineralogical heterogeneity via Fourier transform infrared microscopy. Energy & Fuels, 29(7), pp.4264-4271.
4. Wang, Y., Wang, L.H., Wang, J.Q., Jiang, Z., Jin, C. and Wang, Y.F., 2017. Investigating microstructure of Longmaxi shale in Shizhu area, Sichuan Basin, by optical microscopy, scanning electron microscopy and micro-computed tomography. Nuclear Science and Techniques, 28(11), p.163

5. Yang, T., Li, X. and Zhang, D. 2015. Quantitative dynamic analysis of gas desorption contribution to production in shale gas reservoirs. Journal of Unconventional Oil and Gas Resources, 9, 18–30, doi:10.1016/j.juogr.2014.11.003
6. Ambrose, R.J., Hartman, R.C., Diaz-Campos, M., Akkutlu, Y., Sondergeld, C.H. 2010. New pore-scale considerations for shale gas in place calculations. Paper SPE-131772-MS, Society of Petroleum Engineers. Paper presented at the Petroleum Engineers Unconventional Gas Conference, 23-25 February, Pittsburgh, Pennsylvania, USA.
7. Bai, B., Zhu, R., Wu, S., Yang, W., Gelb, J., Gu, A., Zhang, X. and Su, L. 2013. Multi-scale method of Nano (Micro)-CT study on microscopic pore structure of tight sandstone of Yanchang Formation, Ordos Basin. Petroleum Exploration and Development, 40(3), 354–358, doi:10.1016/S1876-3804(13)60042-7.
8. Curtis, M., Ambrose, R., Sondergeld, C., 2010. Structural characterization of gas shales on the micro-and nano-scales. Paper SPE-137693-MS, Society of Petroleum Engineers. Paper presented at the Canadian Unconventional Resources and International Petroleum Conference, 19-21 October, Calgary, Alberta, Canada.
9. Heller, R., and Zoback, M. 2014. Adsorption of methane and carbon dioxide on gas shale and pure mineral samples. Journal of Unconventional Oil and Gas Resources, 8, 14–24, doi:10.1016/j.juogr.2014.06.001.
10. Cui, X., Bustin, A. and Bustin, R. M. 2009. Measurements of gas permeability and diffusivity of tight reservoir rocks: Different approaches and their applications. Geofluids, 9(3), 208–223, doi:10.1111/j.1468-8123.2009.00244.x.
11. Dicker, A. and Smits, R. 1988. A practical approach for determining permeability from laboratory pressure-pulse decay measurements. Paper SPE-17578-MS, Society of Petroleum Engineers. Paper presented at the International Meeting on Petroleum Engineering, 1–4 November, Tianjin, China.
12. Jones, S. 1997. A technique for faster pulse-decay permeability measurements in tight rocks. SPE Formation Evaluation, 12(1), 19–26, doi:10.2118/ 28450-PA.
13. Kwon, O., Kronenberg, A. K., Gangi, A. F. and Johnson, B. 2001. Permeability of Wilcox shale and its effective pressure law. Journal of Geophysical Research, 106(B9), 19,339–19,353, doi: 10.1029/2001JB000273.
14. Kwon, O., Kronenberg, A.K., Gangi, A.F., Johnson, B. and Herbert, B.E., 2004. Permeability of illite-bearing shale: 1. Anisotropy and effects of clay content and loading. Journal of Geophysical Research: Solid Earth, 109(B10).
15. Ma, Y., Pan, Z., Zhong, N., Connell, L. D., Down, D. I., Lin, W. and Zhang, Y. 2016. Experimental study of anisotropic gas permeability and its relationship with fracture structure of Longmaxi Shales, Sichuan Basin, China. Fuel, 180, 106–115, doi:10.1016/j.fuel.2016.04.029.
16. Pan, Z., Ma, Y., Connell, L. D., Down, D. I. and Camilleri, M. 2015. Measuring anisotropic permeability using a cubic shale sample in a triaxial cell. Journal of Natural Gas Science and Engineering, 26, 336–344, doi:10.1016/j.jngse.2015.05.036.
17. Fisher, Q., Lorinczi, P., Grattoni, C., Rybalcenko, K., Crook, A. J., Allshorn, S., Burns, A. D. & Shafagh, I. 2017. Laboratory characterization of the porosity and permeability of gas shales using the crushed shale method: Insights from experiments and numerical modelling. Marine and Petroleum Geology, 86, 95-110.

18. Luffel, D. and Guidry, F. 1992. New core analysis methods for measuring reservoir rock properties of Devonian shale. Journal of Petroleum Technology, 44(11), 1184–1190, doi:10.2118/20571-PA.
19. Luffel, D., Hopkins, C. and Schettler, P. Jr. 1993. Matrix permeability measurement of gas productive shales. Paper SPE-26633-MS, Society of Petroleum Engineers. Paper presented at SPE Annual Technical Conference and Exhibition, 3–6 October, Houston, Texas.
20. Josh, M., Esteban, L., Delle Piane, C., Sarout, J., Dewhurst, D. N. and Clennell, M. B. 2012. Laboratory characterisation of shale properties, Journal of Petroleum Science and Engineering, 88–89, 107–124, doi:10.1016/j.petrol.2012.01.023
21. Loucks, R. G., Reed, R. M., Ruppel, S. C. and Hammes, U. 2012. Spectrum of pore types and networks in mudrocks and a descriptive classification for matrix-related mudrock pores, AAPG Bulletin, 96(6), 1071–1098, doi:10.1306/08171111061.
22. Chalmers, G. R., Bustin, R. M. and Power, I. M. 2012. Characterization of gas shale pore systems by porosimetry, pycnometry, surface area, and field emission scanning electron microscopy/transmission electron microscopy image analyses: Examples from the Barnett, Woodford, Haynesville, Marcellus, and Doig units. AAPG Bulletin, 96(6), 1099–1119, doi:10.1306/10171111052.
23. Ma, L., Dowey, P. J., Rutter, E., Taylor, K. G. & Lee, P. D. 2019. A novel upscaling procedure for characterising heterogeneous shale porosity from nanometer-to millimetre-scale in 3D. Energy, 181, 1285-1297.
24. Curtis, M.E., Ambrose, R.J., Sondergeld, C.H. and Rai, C.S. 2011. Investigation of the relationship between organic porosity and thermal maturity in the Marcellus Shale. Paper SPE-144370-MS, Society of Petroleum Engineers. Paper presented at the North American Unconventional Gas Conference and Exhibition, 14-16 June, The Woodlands, Texas, USA.
25. Long, H., Swennen, R., Foubert, A., Dierick, M. and Jacobs, P. 2009. 3-D quantification of mineral components and porosity distribution in Westphalian C sandstone by microfocus X-ray computed tomography. Sedimentary Geology, 220, 116-125.
26. Sakellariou, A., Sawkins, T.J., Senden, T.J., Arns, C.H., Limaye, A., Sheppard, A.P., Sok, R.M., Knackstedt, M.A., Pinczewski, W.V., Berge, L.I. and Øren, P.E. 2003. Micro-CT facility for imaging reservoir rocks at pore scales. SEG Annual Meeting, Dallas, Texas, October 26-31.
27. Garum, M., Glover, P.W.J., Lorinczi, P., Drummond-Brydson, R., Hassanpour, A. 2020. Micro- and nano-scale pore structure in gas shale using Xμ-CT and FIB-SEM techniques. In press (Energy and Fuel).
28. Akbarabadi, M., Saraji, S., Piri, M., Georgi, D. & Delshad, M. 2017. Nano-scale experimental investigation of in-situ wettability and spontaneous imbibition in ultra-tight reservoir rocks. Advances in Water Resources, 107, 160-179.
29. Garum, M., Paul, GWJ, Lorinczi P., and Hassanpour, A. 2020. Investigation of Nano-Scale Structures by Using Nano-CT and FIB-SEM Approaches to Characterizing of Gas Shale, 82nd EAGE Annual Conference & Exhibition Workshop Programme, 2020, 1 – 5.
30. Boruah, A. & Ganapathi, S. 2015. Microstructure and pore system analysis of Barren Measures shale of Raniganj field, India. Journal of Natural Gas Science and Engineering, 26, 427-437.
31. Iassonov, P., Gebrenegus, T., Tuller, M. 2009. Segmentation of x-ray computed tomography images of porous materials: a crucial step for characterization and quantitative analysis of pore structures. Water Resources Research, 45, W09415. http:// dx.doi.org/10.1029/20 09WR0 08087.

32. Gundermann, T. & Odenbach, S. 2014. Investigation of the motion of particles in magnetorheological elastomers by X-µCT. Smart Materials and Structures, 23.
33. Igarashi, T., Shono, N., Kin, T. & Saito, T. 2016. Interactive Volume Segmentation with Threshold Field Painting. Proceedings of the 29th Annual Symposium on User Interface Software and Technology - UIST '16.
34. Busch, A., Schweinar, K., Kampman, N., Coorn, A., Pipich, V., Feoktystov, A., Leu, L., Amann-Hildenbrand, A. & Bertier, P. 2017. Determining the porosity of mudrocks using methodological pluralism. Geological Society, London, Special Publications, 454, 15-38.
35. Washburn, E.W. Note on a method of determining the distribution of pore sizes in a porous material. Proc. Natl. Acad. Sci. USA 1921, 7, 115–116
36. Webb, P.A. 2001. An introduction to the physical characterization of materials by mercury intrusion porosimetry with emphasis on reduction and presentation of experimental data. Volume and Density for Particle Technologists. Micromeritics Instrument.
37. Peng, S., Hu, Q., Dultz, S. & Zhang, M. 2012. Using X-ray computed tomography in pore structure characterization for a Berea sandstone: Resolution effect. Journal of Hydrology, 472-473, 254-261.
38. Bear, J. 1988. Dynamics of Fluids in Porous Media, Courier Corp., New York.
39. Lorinczi, P., Burns, A. D., Lesnic, D., Fisher, Q. J., Crook, A. J., Grattoni, C. & Rybalcenko, K. 2014. Direct and Inverse Methods for Determining Gas Flow Properties of Shale. Paper SPE-167750-MS, Society of Petroleum Engineers. Paper presented at the SPE/EAGE European Unconventional Resources Conference and Exhibition, 25-27 February, Vienna, Austria.
40. Zamirian, M., Aminian, K.K., Ameri, S., Fathi, E. 2014. New steady-state technique for measuring shale core plug permeability. In: SPE/ CSUR unconventional. resources conference—Canada. Society of Petroleum Engineers.
41. Passey, Q.R., Bohacs, K., Esch, W.L., Klimentidis, R. and Sinha, S., 2010. From oil-prone source rock to gas-producing shale reservoir-geologic and petrophysical characterization of unconventional shale gas reservoirs. In International Oil and Gas Conference and Exhibition in China. Society of Petroleum Engineers.
42. Washburn, K.E., Birdwell, J.E., Foster, M. and Gutierrez, F., 2015. Detailed description of oil shale organic and mineralogical heterogeneity via Fourier transform infrared microscopy. Energy & Fuels, 29(7), pp.4264-4271.
43. Wang, Y., Wang, L.H., Wang, J.Q., Jiang, Z., Jin, C. and Wang, Y.F., 2017. Investigating microstructure of Longmaxi shale in Shizhu area, Sichuan Basin, by optical microscopy, scanning electron microscopy and micro-computed tomography. Nuclear Science and Techniques, 28(11), p.163.
44. Seaton, N.A. and Walton, J.P.R.B., 1989. A new analysis method for the determination of the pore size distribution of porous carbons from nitrogen adsorption measurements. Carbon, 27(6), pp. 853-861.
45. Jennings, B.R., Parslow, K., 1988. Particle Size Measurement: The Equivalent Spherical Diameter. Proceedings of the Royal Society of London A: Mathematical, Physical and Engineering Sciences. Vol. 419. No. 1856.
46. Yang, Y. & Bao, F. 2017. Characteristics of shale nanopore system and its internal gas flow: A case study of the lower Silurian Longmaxi Formation shale from Sichuan Basin, China. Journal of Natural Gas Geoscience, 2, 303-311.

47. Busch, A., Schweinar, K., Kampman, N., Coorn, A., Pipich, V., Feoktystov, A., Leu, L., Amann-Hildenbrand, A. and Bertier, P., 2017. Determining the porosity of mudrocks using methodological pluralism. Geological Society, London, Special Publications, 454(1), pp.15-38.
48. Ewing, R.P., Horton, R., 2002. Diffusion in sparsely connected porespaces: temporal and spatial scaling. Water Resources Research, 38 (12), 1285.
49. Glover, P.W.J. and Walker, E. 2009. Grain size to effective pore size transformation derived from an electro-kinetic theory. Geophysics, 74(1), E17-E29.
50. Washburn, K.E., Birdwell, J.E., Foster, M. and Gutierrez, F., 2015. Detailed description of oil shale organic and mineralogical heterogeneity via Fourier transform infrared microscopy. Energy & Fuels, 29(7), pp.4264-4271.
51. Wang, Y., Wang, L.H., Wang, J.Q., Jiang, Z., Jin, C. and Wang, Y.F., 2017. Investigating microstructure of Longmaxi shale in Shizhu area, Sichuan Basin, by optical microscopy, scanning electron microscopy and micro-computed tomography. Nuclear Science and Techniques, 28(11), p.163.
52. Seaton, N.A. and Walton, J.P.R.B., 1989. A new analysis method for the determination of the pore size distribution of porous carbons from nitrogen adsorption measurements. Carbon, 27(6), pp. 853-861.
53. Bertier, P., Schweinar, K., Stanjek, H., Ghanizadeh, A.M.I.N., Clarkson, C.R., Busch, A., Kampman, N., Prinz, D., Amann-Hildenbrand, A., Krooss, B.M. and Pipich, V., 2016. On the use and abuse of N2 physisorption for the characterization of the pore structure of shales. In The clay minerals society workshop lectures series (Vol. 21, pp. 151-161).
54. Lowell, S., Shields, J.E., Thomas, M.A. and Thommes, M., 2012. Characterization of porous solids and powders: surface area, pore size and density (Vol. 16). Springer Science & Business Media.
55. Sakhaee-Pour, A. and Bryant, S., 2012. Gas Permeability of Shale. SPE Reservoir Evaluation and Engineering, Paper SPE 146944, pp. 401-409.
56. Yan, F. & Han, D.-H. 2013. Measurement of elastic properties of kerogen. SEG Technical Program Expanded Abstracts 2013. Society of Exploration Geophysicists.
57. Chung, T., Wang, Y.D., Armstrong, R.T. and Mostaghimi, P. 2019. Approximating Permeability of Microcomputed-Tomography Images Using Elliptic Flow Equations. Paper SPE 191379, Society of Petroleum Engineers. doi:10.2118/191379-PA.
58. Begg, S.H. and King, P.R. 1985. Modelling the Effects of Shales on Reservoir Performance: Calculation of Effective Vertical Permeability. Paper SPE 13529, Society of Petroleum Engineers. doi:10.2118/13529-MS.
59. Begg, S.H., Carter, R.R. and Dranfield, P. 1989. Assigning Effective Values to Simulator Gridblock Parameters for Heterogeneous Reservoirs, Paper SPE 16754, Society of Petroleum Engineers. doi:10.2118/16754-PA.
60. Peng, S., Yang, J., Xiao, X., Loucks, B., Ruppel, S.C. and Zhang, T., 2015. An integrated method for upscaling pore-network characterization and permeability estimation: example from the Mississippian Barnett Shale. Transport in Porous Media, 109(2), pp. 359-376.
61. Zhang, S., Klimentidis, R.E. and Barthelemy, P., 2012, August. Micron to millimeter upscaling of shale rock properties based on 3D imaging and modeling. In International Symposium of the Society of Core Analysts (Vol. 27, p. 30).
62. Akkutlu, I.Y. and Fathi, E., 2012. Multiscale gas transport in shales with local kerogen heterogeneities. SPE Journal, 17(04), pp. 1-002.

63. Shabro, V, Torres-Verdin, C., Javadpour, F. and Spehrnoori, K. 2012. Finite-Difference Approximation for Fluid-Flow Simulation and Calculation of Permeability in Porous Media, Transport in Porous Media, 94, 775-793. doi: 10.1007/s11242-012-0024-y
64. Ajiz, M.A. and Jennings, A. 1984. A robust incomplete Choleski-conjugate gradient algorithm. International Journal of Numerical Methods in Engineering, 20: 949-966. doi:10.1002/nme.1620200511
65. Johnson, D.L., Koplik, J. and Schwartz, L.M. 1986. New pore-size parameter characterizing transport in porous media: Physical Review Letters, 57(20), 2564–2567, http://dx.doi.org/10.1103/PhysRevLett.57.2564
66. Glover P.W.J. (2015). Geophysical Properties of the Near Surface Earth: Electrical Properties, In: Gerald Schubert (editor-in-chief) Treatise on Geophysics, 2nd edition, Vol 11. Oxford: Elsevier, 89-137.
67. Glover P.W.J. (2010). A generalised Archie's law for n phases: Geophysics, 75(6), E247-E265, doi: 10.1190/1.3509781.
68. Revil, A., and Cathles, L.M. 1999. Permeability of shaly sands: Water Resources Research, 35(3), 651-662.
69. Milliken, K.L., Rudnicki, M., Awwiller, D.N., Zhang, T. 2013. Organic matter-hosted poresystem, Marcellus Formation (Devonian), Pennsylvania. AAPG Bulletin, 97, 177–200.
70. Akkutlu, I. Y. & Fathi, E. 2012. Multiscale gas transport in shales with local kerogen heterogeneities. Paper SPE-146422-PA, Society of Petroleum Engineers. SPE Journal, 17 (4), 1002-1011.
71. Javadpour, F., Fisher, D. & Unsworth, M. 2007. Nanoscale gas flow in shale gas sediments. Journal of Canadian Petroleum Technology, 46 (10).
72. Ambrose, R.J., Hartman, R.C., Diaz-Campos, M., Akkutlu, I.Y., Sondergeld, C.H. 2012. Shale gas-in-place calculations Part I: new pore-scale considerations. Paper SPE-131772-PA, Society of Petroleum Engineers. SPE Journal, 17 (1).
73. Wang, S., Pomerantz, A. E., Xu, W., Lukyanov, A., Kleinberg, R. L. & Wu, Y.-S. 2017. The impact of kerogen properties on shale gas production: A reservoir simulation sensitivity analysis. Journal of Natural Gas Science and Engineering, 48, 13-23.
74. Ma, L., Taylor, K. G., Lee, P. D., Dobson, K. J., Dowey, P. J. & Courtois, L. 2016. Novel 3D centimetre-to nano-scale quantification of an organic-rich mudstone: The Carboniferous Bowland Shale, Northern England. Marine and Petroleum Geology, 72, 193-205.
75. Ma, L., Slater, T., Dowey, P. J., Yue, S., Rutter, E. H., Taylor, K. G. & Lee, P. D. 2018. Hierarchical integration of porosity in shales. Scientific Reports, 8, 11683.
76. Saif, T., Lin, Q., Butcher, A. R., Bijeljic, B. & Blunt, M. J. 2017. Multi-scale multi-dimensional microstructure imaging of oil shale pyrolysis using X-ray micro-tomography, automated ultra-high resolution SEM, MAPS Mineralogy and FIB-SEM. Applied Energy, 202, 628-647.